This is a preprint, the final version is subject to change, of the American Mineralogist (MSA)
Cite as Authors (Year) Title. American Mineralogist, in press.
DOI: https://doi.org/10.2138/am-2018-6424

Nanoscale partitioning of Ru, Ir and Pt in base-metal sulfides from the Caridad chromite deposit, Cuba

José M. González-Jiménez[a], Artur Deditius[b], Fernando Gervilla[a,c], Martin Reich[d], Alexandra Suvorova[e], Malcolm P. Roberts[e], Josep Roqué[f], Joaquín A. Proenza[f]

a. Departamento de Mineralogía y Petrología, Facultad de Ciencias, Universidad de Granada, Avda. Fuentenueva s/n, 18002 Granada, Spain.
b. School of Engineering and Information Technology, Murdoch University, Murdoch, 6150 WA, Australia.
c. Instituto Andaluz de Ciencias de la Tierra (IACT), CSIC-UGR, Avda. de las Palmeras 4, 18100 Armilla, Granada, Spain.
d. Department of Geology and Andean Geothermal Center of Excellence (CEGA), FCFM, Universidad de Chile, Plaza Ercilla 803, Santiago, Chile.
e. Centre for Microscopy, Characterisation and Analysis (CMCA), The University of Western Australia, Perth, 6009 WA, Australia.
f. Departament de Mineralogia, Petrologia i Geologia Aplicada, Universitat de Barcelona (UB), 08028 Barcelona, Spain.

Submitted
to
American Mineralogist
Special issue "Applications of Fluid, Mineral, and Melt Inclusions"

REVISION 1

*Corresponding author: José María González Jiménez
Address: Departamento de Mineralogía y Petrología, Facultad de Ciencias, Universidad de Granada, Granada, Spain
Avda. Fuentenueva s/n 18002 Granada
Phone: +34 958 246 619
E-mail: jmgonzj@ugr.es

Abstract

We report new results of a combined focused ion beam and high-resolution transmission electron microscopy (FIB/HRTEM) investigation of platinum-group elements (PGE)-rich base-metal sulfides. The Ni-Fe-Cu base-metal sulfides (BMS) studied are millerite [NiS], pentlandite [$(Ni,Fe)_9S_8$], pyrite [FeS_2] and chalcopyrite [$CuFeS_2$]. These BMS were found forming composite inclusions (<60 μm across) within larger unaltered chromite from the Caridad chromite deposit, which is hosted in the mantle section of the Mayarí-Baracoa Ophiolite in eastern Cuba. Electron probe microanalysis revealed of BMS revealed PGE values of up to 1.3 wt.%, except for pentlandite grains where PGE concentrations can reach up to 12.8 wt.%. Based on the amount of Ru, two types of pentlandite are defined: (1) Ru-rich pentlandite with up to 8.7 wt.% of Ru and <3.5 wt.% of Os, and (2) Ru-poor pentlandite with Ru <0.4 wt.% and Os <0.2 wt.%. Ru-rich pentlandite contains Ir-Pt nanoparticles whereas the other sulfides do not host nanometer-sized platinum-group minerals (PGM). The Ir-Pt inclusions are found as: (1) idiomorphic, needle-shape (acicular) nanoparticles up to 500 nm occurring along the grain boundaries between Ru-rich pentlandite and millerite, and (2) nanospherical inclusions (<250 nm) dispersed through the matrix of Ru-rich pentlandite. HRTEM observations and analysis of the selected area electron diffraction patterns revealed that nanoparticles of Ir-Pt form domains within Ru-rich pentlandite. Fast Fourier transform analyses of the HRTEM images showed epitaxy between Ir-Pt domain and PGE-poor millerite, which argues for oriented growth of the latter phase. These observations point to sub-solidus exsolution of the Ir-Pt alloy, although the presence of nanospherical Ir-Pt inclusions in some other grains suggest the possibility that Ir-Pt nanoparticles formed in the silicate melt before sulfide liquid immiscibility. These Ir-Pt nanocrystals were later collected by the sulfide melt, preceding the formation of Ru-rich pentlandite. Early crystallization of the Ru-rich pentlandite and Ir-Pt nanoparticles led to the efficient scavenging of PGE from the melt, leaving a PGE-poor sulfide residue composed of millerite, pyrite, chalcopyrite and a second generation of PGE-poor pentlandite.

Keywords: nanoparticles, platinum-group elements (PGE), focused-ion beam (FIB), transmission electron microscopy (TEM), chromite, Cuba

INTRODUCTION

The potential role of nanometer-sized phases during the selective partitioning of platinum-group elements (PGE: Os, Ir, Ru, Rh, Pt and Pd) has been little explored, particularly under the high temperatures that are typical for magmatic processes. Previous experimental studies carried out in binary mixtures of pure metals indicate that Ir and Pt can form alloys with a face-centered cubic (fcc) structure over a range of temperatures ranging from 975 to 1370 °C (Turchi et al. 2006 and references therein). This is consistent with the fact that Pt-bearing Ir alloys phases have been indeed documented in natural samples. For example, Pt-bearing Ir alloys (with trace amounts of Os) have been found associated with laurite [RuS_2] or pentlandite [$(Ni,Fe)_9S_8$] in mantle peridotites (e.g., Lherz massif in France and Horoman Complex in Japan; Kogiso et al. 2008; Lorand et al. 2010), chromite ores from the Oman ophiolite (Ahmed and Arai 2003) and in magmatic platinum-group mineral nuggets found in rivers draining ultramafic-mafic complexes of the Goodnews Bay in Alaska (e.g., Tolstykh et al. 2002). Additionally, nanometer-sized particles of Ir-bearing Pt alloys have been observed within pentlandite grains in chromite ores from the Bushveld Complex in South Africa (Wirth et al. 2013).

Experimental studies by Peregoedova et al. (2004) show that monosulfide solid solution (*mss*) with variable amounts of Pt, Ir and Pd can exsolve discrete Ir-Pt alloys particles during desulfurization (i.e., decrease of sulfur fugacity, f_{S_2}) at magmatic temperatures (~1000 °C). Based on this observation, Luguet and Reisberg (2016) suggested that Ir-Pt-(Os) alloys associated with BMS in mantle peridotite were most likely exsolved from a precursor PGE-bearing *mss,* which had experienced desulfurization at high-temperatures during partial melting. The exsolution of (sub)-micrometric Ir-Pt-(Os) from base-metal sulfides may have also resulted from desulfurization of a PGE-bearing *mss* due to redox changes of the mantle (Jugo, 2009) or interaction with percolating S-undersaturated melt/fluids (Lorand et al. 2010). In contrast, experiments in the Fe-Cu-S-(Pt+As) system and mineralogical observation of PGE ores from the Bushveld Complex provide evidence that Pt-rich nanoparticle formation may precede crystallization of the host *mss* (Helmy et al. 2013; Wirth et al. 2013; Junge et al. 2015). More recently, Fonseca et al. (2017) reported the formation of Ir-Pt alloys (>100 μm across) in equilibrium with Ni-rich sulfide melts during

experiments. These observations suggest that Ir-Pt alloys may crystallize directly from silicate melts, either before or contemporaneously with the segregation of immiscible sulfide melts. In fact, Finnigan et al. (2008) synthesized nanometer-sized Ir-Pt nanocrystals from basaltic melts in experiments involving the crystallization of chromite, at the P-T-f_{O_2} conditions relevant for the formation of chromite deposits in the upper mantle (i.e., 0.5 GPa T ~ 1300-1400 °C and f_{O_2} at FMQ; see Figure 4a in Finnigan et al. 2008). However, it is important to note the aforementioned experiment was carried out in the absence of sulfur, therefore hindering the formation of Ir-Pt alloys within sulfides.

The previous data show that the relationship between Pt-rich Ir alloys and magmatic sulfides is still poorly understood. In particular, the mechanism(s) and relative timing of Ir-Pt alloy crystallization during magmatic evolution remains elusive, in particular when sulfides are present. This contribution aims to fill this gap of knowledge by providing a detailed characterization of a suite of micrometer to nano-meter-sized Ir-Pt alloy inclusions hosted within Ni-rich sulfides from the Caridad chromite deposit in eastern Cuba. This study stems from a recent report by González-Jiménez and Reich (2017) reporting the occurrence of Ir-Pt nanoalloys at the interface between pentlandite and secondary heazlewoodite [Ni_3S_2] in the altered zones of the chromitite from this deposit. These aforementioned authors preliminarily suggested a magmatic origin for these nanoalloys, although this hypothesis was not confirmed on the basis of the available data. Here we present a nanoscale characterization of the Ir-Pt alloy inclusions and the sulfide host matrix, obtained by combining focused ion beam micro-sampling techniques with high-resolution transmission electron microscopy (HRTEM) observations and electron microprobe analysis (EPMA). Our study explores the origin of Ir-Pt nanoparticles in natural samples, providing new insights to unravel the often complex relations between noble metal alloy formation, sulfide melt segregation and chromite crystallization in high-temperature ore system.

SAMPLES AND METHODS

The samples analyzed in this study were collected from the podiform chromitite ore body of Caridad in the Sagua de Tánamo district, eastern Cuba (Fig. 1; Proenza et al. 1999; Gervilla et al. 2005; González-Jiménez et al. 2011, 2012).

The Sagua de Tánamo area is a small mining district (~3 km long), located in the northern part of the Mayarí-Cristal massif which, together with the Moa-Baracoa massif to the east, constitute the Mayarí-Baracoa Ophiolitic Belt (MBOB) (Marchesi et al. 2006; Proenza et al. 2006). The Mayarí-Cristal massif represents a piece of mantle wedge suprasubduction-zone, which formed close to the Greater Antilles paleo-island arc 90 Ma ago (Proenza et al. 2006; Marchesi et al. 2006, 2007, 2011). The mantle sequence of the Mayarí-Cristal massif consists mainly of highly depleted harzburgite and subordinate concordant lenses and layers of dunite, all intensively serpentinized (Proenza et al. 2003). Dykes of gabbros and pyroxenites with island arc tholeiitic affinity crosscut these peridotites (Marchesi et al. 2006). The Caridad chromitite body is hosted in a dunite lens lying concordantly with this mantle harzburgite. The samples analyzed in this study are banded-textured chromitites collected from the external part of the ore body; they are almost entirely unaltered, although some chromite grains exhibit narrow alteration to ferrian chromite along edges or late crosscutting fractures filled with serpentine. In order to ensure a magmatic origin of PGM inclusions, this study focused exclusively in grains that were fully hosted in unaltered chromite.

Compositional analyses of the PGE-bearing inclusions and their host sulfides were acquired using a JEOL 8530F electron probe microanalyzer (EPMA) equipped with five tunable wavelength dispersive spectrometers at the Centre of Microscopy, Characterisation and Analysis (CMCA), University of Western Australia. Operating conditions were 40° take-off angle, an accelerating voltage of 20 kV, a beam current of 20 nA, with the beam fully focused to 1 μm diameter. Elemental data were acquired during two analytical sessions. The following analyzing crystals were used: LiF for Fe Kα, Ru Lα, Te Lα, Cu Kα, Ni Kα, Co Kα, Cr Kα, Sn Lα, Hg Lα, Re Lα, Os Lα, Ir Lα, Pt Lα, PETJ for Rh Lα, S Kα, Ag Lα, Pd Lα, Ru Lα, PETH for Mo Lα, Pb Mα, Sb Lα, Bi Mα, and TAP for Si Kα, As Lα, Se Lα. The counting time was 20-30 s for all elements and Mean Atomic Number (MAN) background correction was used for all elements (Donovan et al. 1996, 2016). The standards were Cr_2O_3 for Cr Kα, galena for Pb Mα, Bi_2Se_3 for Se Lα, Ag metal for Ag Lα, Cu metal for Cu Kα, wollastonite for Si Kα, Mo metal for Mo Lα, Co metal for Co Kα, Bi metal for Bi Mα, Pt metal for Pt Lα, metal Sb for Sb Lα, arsenopyrite (Asp200) for As Lα, cassiterite for Sn Lα, Au metal for Au Lα, millerite for S Kα, Ni Kα,

chalcopyrite for Fe Kα, Ru metal for Ru Lα, Rh metal for Rh Lα, Pd metal for Pd Lα, Os metal for Os Lα, Ir metal for Ir Lα, Re metal for Re Lα, and synthetic HgTe (coloradoite) for Te Lα, Hg Lα. On peak interference corrections were applied as appropriate (Donovan et al. 1993). Unknown and standard intensities were corrected for deadtime. For both sessions, a quantitative blank correction was utilized (Donovan et al. 2011). The Phi-Rho-Z algorithm utilized was Armstrong/Love Scott (Armstrong, 1988). Maximum detection limits for each element are provided in Table S1.

Elemental mapping were acquired at an accelerating voltage of 20 kV and a beam current of 80 nA. Pixel dimensions were between 0.25 and 0.10 μm, depending on the size of the grain of interest. The dwell time per pixel was 200 ms. The calibration run used for map post-acquisition processing was similar to that for the point analyses given above. The raw count data was processed using the Calcimage® application and output for further enhancement using Golden Software's Surfer® program. Maximum detection limits for the analyzed elements were: S = 0.2 wt.%, Fe = 0.1-0.15 wt.%, Cu = 0.2-1.0 wt.%, As = 0.3-0.4 wt.%, Ir = 0.8-1.0 wt.%, Ru = 0.4-0.6 wt.%, Rh = 0.3-0.4 wt.%, Pt = 0.8-1.0 wt.%, Pd = 0.3-0.4 wt.%.

In-situ Re-Os analyes of the BMS were carried out by González-Jiménez et al. (2012) at GEMOC (Macquarie University, Australia) using Wave/Merchantek UP 213 laser microprobe with a modified ablation cell coupled with a Nu Plasma Multicollector ICP-MS. Measurements were made in static collection mode by using two combinations of collectors: (1) masses 194, 192, 190, 189, 188, 187, 186, and 185 in Faraday cups, and (2) masses 194, 193, 192, 191, 190, 189, 188, and 186 in Faraday cups and 187 and 185 in ion counters. The all-Faraday configuration allows the simultaneous measurement of Os, Re, and Pt, and the repositioning of the ion beams by changing the magnet field and zoom lens voltages to direct masses 187 and 185 into ion counters allows Ir to be measured. During the analyses the laser was fired at a frequency of 5 Hz, with energies of 1–2 mJ/pulse and a spot size of 20–80 μm. A standard NiS bead (PGE-A) with 199 ppm Os (Lorand and Alard, 2001) and $^{187}Os/^{188}Os = 0.1064$ (Pearson et al., 2002) was analyzed between samples to monitor any drift in the Faraday cups and ion counters. These variations typically were less than 0.1 % over a long day's analytical session. During the analyses, a dry aerosol of

Ir was bled into the gas line between the ablation cell and the ICP-MS to provide a mass-bias correction with a precision independent of the abundance of Os in the unknown. The data were collected using the Nu Plasma time-resolved software, which allows the selection of the most stable intervals of the signal for integration. The selected interval was divided into 40 replicates to provide a measure of the standard error. Under the ablation conditions described above, signal intensities (0.02–1.4 V) obtained give a range of precision for $^{187}Os/^{188}Os$ from 2×10^{-4} to 2×10^{-3} (2SE); these values are quite similar to, or better than, that obtained for the PGE-A standard.

The thin-foil samples were prepared by using FEI Helios NanoLab G3 CX DualBeam and focused ion beam (FIB) at the Center for Microscopy, Characterization and Analysis (CMCA), University of Western Australia. Sections prepared using the Helios G3 were extracted from the sample surface by in-situ lift-out, welded onto a copper grid, thinned to electron transparency with a 30 kV ion beam where the beam current was progressively reduced from 2.5 nA to 0.23 nA, and then finally polished with a 5 kV beam with a 41 pA current. Subsequently, the samples were analysed by using a Titan G2 80-2090 transmission electron microscope (TEM) with ChemiSTEM technology at 200 kV.

RESULTS

Base-metal sulfide assemblages

The BMS studied here include millerite [NiS)], pentlandite [$(Ni,Fe)_9S_8$], pyrite [FeS_2] and chalcopyrite [$CuFeS_2$] (Figs. 2-4). They form isolated grains enclosed by unaltered magmatic chromite away from visible fractures or the contact with the serpentinized silicate matrix of the chromitite (Fig. 2a-h). The BMS inclusions are up to 60 μm across and have polyhedral (rarely spherical) shape and sharp boundaries with the host chromite. Sporadically, millerite occurs as single isolated grains. Polyphase aggregates consist of millerite associated with pentlandite ± Ru-rich pentlandite ± pyrite ± chalcopyrite (Fig. 2a-d), whereas the biphasic ones consist of millerite with pentlandite, pyrite or chalcopyrite (Fig. 2c-h). Interestingly, pyrite is found as bleb-like inclusions in millerite grains or at their rims; the latter microstructural position is also characteristic of chalcopyrite.

Quantitative WDS X-ray element maps also reveal differences of PGE contents in the individual sulfide grains forming a given composite solid inclusion (Fig. 3). These noble metals are distributed homogenously within the matrix of the hosting minerals or form submicron-sized particles of mainly Ir and Pt (Fig. 3).

Table S1 and Figure 4a-f show results of EPMA analyses BMS. All the analyzed base-metal sulfides show Fe, Ni, Cu, and S close to ideal stoichiometry and overall total PGE concentrations up to 1.3 wt.%, with the exception of a few Ru-rich pentlandite grains (up to 12.8 wt.%; Table S1 and Fig. 4c-f). Based on their Ru content, two types of pentlandite were identified, Ru-rich and Ru-poor, were identified. The Ru-rich pentlandite is richer in Ru and Os (up to 8.67 wt.% and 3.53 wt.% respectively) than Ru-poor pentlandite (Ru <0.4 wt.% and Os <0.2 wt.%; Fig. 4c-d). Millerite contains up to 3 wt.% of Fe, 0.07 wt.% of Os and Ru and 0.05 wt.% of Rh (Fig. 4e). Pentlandite (up to 42.2 wt.% of Ni) is characterized by a moderate variation in Ni/Fe ratios (1.6-2.1). Pyrite has up to 0.08 wt.% of Os and 0.05 wt.% of Ru; the concentration of Au in pyrite is as high as 0.12 wt.%. Chalcopyrite also is depleted in Ir, Pt and Pd; however, it has the highest contents of Rh (up to 0.4 wt.%). Osmium and Ru in chalcopyrite are up to 0.7 wt.% and <0.07 wt.%, respectively (Table S1).

Structure of platinum-group minerals and base-metal sulfides

The re-examination of the time-resolved spectra signals collected during LA-MC-ICP-MS analyses of Re-Os isotopes of the same samples by González-Jiménez et al. (2012) revealed the presence of abundant ^{194}Pt spikes (Fig. 5). The ^{194}Pt spikes is noticeable as the signal of main components of the host sulfide decreases rapidly (Fig. 5). This observation is consistent with the BSE images suggesting that Pt-rich alloys are not always fully enclosed by the matrix (Fig. 2b). These are single-phase grains with acicular (up to 10 × 5 μm) and bleb-like (<500 nm) shape that are associated with Ru-rich pentlandite often along the contact between this later Ni-Fe sulfide and millerite (Figs. 2a-b and 3), or single sphere-like nanometer-sized grains (<250 nm) that are widespread throughout the matrix of Ru-rich pentlandite (Fig. 2c-d). WDS X-ray maps obtained by EPMA revealed that these particles contain Ir and Pt.

One FIB thin foil (Figs. 6a-e) was cut perpendicular to the grain boundaries between Ir-Pt alloy, Ru-rich pentlandite, and millerite of the grain shown in Figure 2a and 3a-f. The cross section revealed a triangular shape of Ir-Pt particle, reaching a depth of 250 nm (Fig. 6a). The TEM-EDS elemental mapping of the area containing all three phases revealed a better association between Ir, Pt, Os, and Cu in the Ir-Pt particle. In addition, the particle contains Fe, Co, Ru, and S, although Ni is below detection. All elements in the Ir-Pt particle and within the associated sulfides are homogenously distributed (Fig. 5). Ruthenium and Co are also enriched in Ru-pentlandite relative to millerite (Fig. 6a). The high concentrations in Ru, Co and Fe in the Ir-Pt particle and in the coexisting Ru-rich pentlandite is also reflected by a diffuse contact between both minerals (Figs. 6b and 6d). Bright Field (BF) and High-Resolution (HR) TEM observations, and fast Fourier transform analyses (FFT) of the HRTEM images revealed that all three minerals are crystalline (Figs. 6b-e). Fast Fourier Transformation of the HRTEM images of the Ir-Pt nanoparticle showed that it is a single crystal, similar in its structure to Ru-pentlandite and millerite (Figs. 6c-e). The HRTEM investigations of the grain boundary between the Ir-Pt particle and the Ru-rich pentlandite show continuous lattice fringes within a single crystal, and FFT revealed structural continuity (Fig. 6d). This strongly suggests that Ir-Pt particle is a nanometer-sized domain within the Ru-rich pentlandite. In addition, the relative decrease in the Fe and Ni concentration in Ir-Pt domain compared to the Ru-rich pentlandite matrix suggests that PGE+Co+Cu substitute for Fe and Ni in the Ru-rich pentlandite. Epitaxy was found between the Ir-Pt domain and millerite. However, a small misorientation between the structure of the Ir-Pt domain and millerite is documented by discoidal diffused diffraction maxima (Fig. 6e).

DISCUSSION

Origin of base-metal sulfides

Based on their textural position within chromite it is proposed that BMS were trapped during the formation of the hosting mineral (e.g., Garuti et al. 1999; Malitch et al. 2001; González-Jiménez et al. 2012). The idiomorphic morphology of some of these grains suggest free crystallization from a melt prior to chromite (e.g., Fig. 2b). In contrast, drop-like or anhedral inclusions may indicate their crystallization from liquid or a mixture of liquid and suspended microcrystallites that were mechanically

trapped by growing chromite (e.g., Fig. 2e). These solid inclusions of BMS consist of single isolated grains of millerite, often associated with polyphasic or biphasic aggregates of pentlandite ± pyrite ± chalcopyrite (Fig. 2a-h). Even though immiscible sulfide melts were segregated before or contemporaneously to chromite crystallization (~1000-1200 °C; Hill and Roeder 1974; Ballhaus 1998), most the observed sulfide assemblages were not present during formation, due to the lower thermal stability of pentlandite, pyrite and chalcopyrite (e.g., Kullerud, 1962, 1963; Makovicky et al. 1986; Sugaki and Kitakaze 1998; Ballhaus et al. 2001; Naldret et al. 2009).

Several experiments in the Fe-Ni-S system have shown that a Fe-rich *mss* is the first solid phase to crystallize after the immiscible segregation of a sulfide liquid from a silicate melt above 1000 °C (Fig. 6a; Kullerud 1962, 1963; Chang and Hsieh 1986; Ebel and Naldrett 1996; Fleet 2006). With a temperature decrease to around ~610 °C, the metal excess in the *mss* is exsolved as pentlandite (Fig. 7b). This assemblage of *mss*+pentlandite is stable down to 300 °C, below which the *mss* decomposes into several sulfides of Ni and Fe, including millerite and pyrite that may coexist with pentlandite (Fig. 6c-d; Shewman and Clark 1970; Misra and Fleet 1973; Craig, 1973; Fedorova and Sinyakova 1993). In some of the studied inclusions of the Caridad deposit (e.g., Fig. 2b) millerite, pentlandite and pyrite exhibit mutual contacts suggesting that they have reached equilibrium. Phase relations in the system Fe-Ni-S system predict that this mineral assemblage is stable at ~135-100 °C (Fig. 7d). In contrast, in some other composite inclusions of millerite+pentlandite+pyrite, pyrite occurs as blebby inclusions in millerite, but not in contact with pentlandite. There are different possibilities to explain these textural types.

The first possibility is the incomplete decomposition of the original mss during its subsolidus subsolidus re-equilibrium. Another possible explanation for the presence of blebby pyrites in millerite (e.g., Fig. 2e-g) is that the precursor Fe-rich *mss* has also undergone significant chemical readjustment but through a different fractional pathway. This original Fe-rich *mss* could be depleted in iron before or once it was sealed in chromite. This would occur as result of the preferential partitioning of Fe^{2+} into chromite (Finnigan et al. 2008), either when minute droplets of sulfide melt were segregated along the silicate melt-chromite interface or trapped in the oxide. In this scenario the composition of the *mss* is shifted towards the Ni-S join of the Fe-Ni-

S system (Naldrett et al., 1989; Naldrett et al. 2009), giving rise in an extreme case to a nearly stoichiometric $Ni_{1-x}S$ (Fig. 8a). This phase that may contain up to 5 wt.% Fe has a α-NiS structure, which should have been inverted to the low-temperature millerite structure (i.e., β-α-NiS) at 379 °C (Kullerud and Yund 1962). In this scenario, minute bleb-like pyrite in some millerite grains (e.g., Fig. 2e-g) may reflect an excess of Fe in the Ni-sulfide, which was exsolved at the temperature of the polymorphic change. The same final product could be achieved if millerite had crystallized directly from a sulfide melt instead of a product of high-temperature subsolidus re-equilibration of the *mss*. Metal-sulfide equilibrium in the Ni-Fe-S system (Wood 1987) indicates that the high-temperature polymorph of millerite α-NiS is stable at temperatures (1000-1200 °C) and sulfur fugacity (log f_{S_2} from -0.5 to 1) relevant for the crystallization in the upper mantle (Fig. 8b). Early crystallization of α-NiS directly from melts can explain the presence of single millerite crystals with or without pyrite inclusions. Moreover, crystallites of millerite might have been trapped in solid state together with some volumes of sulfide liquids during the formation of the chromitite by melt mixing (González-Jiménez et al. 2012). In this scenario, solid and liquids may have reacted producing the variety of composite inclusions of millerite (with or without pyrite) ± pentlandite ± chalcopyrite (e.g., Fig. 2a-h). The origin of pentlandite in these latter inclusions may be associated with the partial reaction of the sulfide liquid with the α-NiS phase. In support of this interpretation, a series of experiments (Sugaki and Kitakaze 1998; Kitakaze et al. 2016) have demonstrated that a high-form of pentlandite can be produced as a result of the pseudoperitectic reaction between Ni-rich liquid and *mss* in the Ni-Fe-S system at ~ 870 °C. This high-form of pentlandite coexist with *mss* and/or liquid at ~ 870-739 °C (Fig. 8c), and its re-equilibration persists to temperatures of about 625 °C, below which it undergoes transformation into the low-form of pentlandite.

The association of chalcopyrite with Ni-Fe sulfides in some of the studied composite grains (Fig. 2a, c and e) points to the Cu-rich compositions. Experimental data on the Fe-Ni-Cu system (Craig and Kullerud 1969; Fleet and Pan 1994; Ballhaus et al. 2001) have shown that *mss* is the first phase that crystallizes from a Fe-Ni-Cu sulfide melt once it has separated by liquid immiscibility from a mafic silicate melt (Fig. 9a). At 1000 °C this *mss* coexists with a Cu-rich melt that may incorporate

variable amounts of Ni (Craig and Kullerud 1969; Balhaus et al. 2001). At ~900 °C, the Cu-rich residual liquid crystallizes to intermediate solid solution (*iss*), so at this point there is a Ni-rich portion and a Cu-rich portion (Fig. 9b). According to the experiments of Craig and Kullerud (1969) at 850 °C the *mss* (with up to 30 wt.% Ni) already coexists with chalcopyrite (Fig. 9b), whereas below 850 °C the *mss* breaks down into several sulfides developing a variety of 2- and 3-phase regions. In this system, assemblages made up of α-NiS and chalcopyrite are stable equilibrium ~ 830 °C (Craig and Kullerud 1969 and references therein); these are interpreted as the precursors of the biphasic grains of millerite+chalcopyrite shown in Fig. 2e. As the temperature cools <600 °C, the *mss* recrystallizes to pentlandite giving rise to the assemblages of pentlandite+chalcopyrite assemblage (Fig. 2a).

The above observations suggest that some of the inclusions in the Caridad deposit may have evolved along different fractionation pathways involving the formation of *mss* and *iss* upon cooling. The differences in the mineralogical composition of the sulfide aggregates, namely the presence of chalcopyrite suggests derivation from droplets of immiscible sulfide melts with distinctly different contents of Ni, Fe and Cu, and different metal/sulfur ratios. Once sealed within the chromite, these sulfide melt inclusions would have evolved as individual closed systems, following different fractional pathways depending on the original composition of the primitive sulfide liquid.

Fate of PGE during crystallization of Fe-Ni sulfide inclusions

The textural relationships observed in some composite solid inclusions made up of Ir-Pt domain in Ru-rich pentlandite and other BMS indicate that some of the small droplets of immiscible sulfide melts rich in base metal segregated at high temperature (≥1000 °C) were also enriched in PGE. This observation is also supported by the relatively high PGE contents detected in single-spot analyses and quantitative X-ray maps obtained using EPMA of some of the BMS (Figs. 3 and 4c-f and Table S1). The contents of PGE within a given BMS mineral in Caridad varies from one inclusion to another (Fig. 4c-f and Table S1), thus providing additional support for the hypothesis that several droplets of sulfide melts with their own inherited PGE melt/sulfur ratio were trapped by growing chromite.

In the polyphasic aggregates in Figures 2a and 3a-f, pentlandite in contact with the Ir-Pt domain is enriched in Ru (up to 6200 ppm), whereas the other BMS of the inclusion have PGE concentrations close to or below detection (Table S1). The polyphasic aggregate of millerite+ Ru-rich pentlandite+pyrite+Ir-Pt-(Rh-Cu) of Figures 2b and 3g-l exhibit a similar distribution of PGE, with pentlandite associated with the Ir-Pt domain being enriched in Ru (Fig. 3j) while the other sulfides within the inclusion are strongly depleted in PGE (Fig. 3j-l). TEM observation of Ir-Pt domains shows the same structure and relative enrichment in Co and Ru as the Ru-rich pentlandite matrix (Fig. 6a-e). This suggests that the alloy was separated from the PGE-rich sulfide during cooling. However, the relatively low content of PGE in the sulfide host (<6200 ppm Ru) was not enough to promote the exsolution of Ir-Pt-Ru domains as lamellae with preferred crystallographic orientation. In fact, Ir and Pt are randomly distributed in the sulfide matrix as attest to the fact that Ru-rich pentlandite of the studied FIB foil does not exhibit additional diffraction maxima between the major Bragg reflections. For example, Junge et al. (2015) observed that pentlandite of the Bushveld Complex contain Rh and Ir rich lamellae only in those domains where the concentration of Rh in the pentlandite matrix was as high as 12.3 wt.%. On the other hand, concentrations of Co and PGE (up to 620 ppm Ru in three analyses out of eleven for this grain; Table S1) are about one order of magnitude lower in millerite than in Ru-rich pentlandite, indicating its later crystallization in a system that was already depleted in these elements. This is consistent with the observation that PGE-depleted millerite has the same crystallographic orientation as the Ir-Pt domains within Ru-rich pentlandite, thus indicating epitaxial growth with some structural misfit at the boundary and accumulation of strain (Figs. 6b and e).

The TEM observations show that the Ru-rich pentlandite containing the Ir-Pt domain fractionated the PGE available into solid solution during the early crystallization stages, leaving behind a PGE-depleted BMS residue. At the Caridad deposit, the PGE originally contained in the silicate melt were mostly fractionated into droplets of immiscible sulfide melt, containing Ni, Fe, Cu, after sulfide saturation. Under equilibrium conditions, the PGE concentrations of the sulfide droplets are estimated to be at least 10,000 times higher than in the coexisting silicate melt (Fleet et al. 1999; Holwell et al. 2015). Furthermore, *mss*/sulfide melt partition coefficient (Li et al. 1996; Ballhaus et al. 2001; Mungall et al. 2005) and empirical

observations in several Ni-Cu and PGE ore deposits (Holwell and MacDonald, 2010; Piña et al. 2012, 2016; Barnes and Ripley, 2015), suggest that the IPGE (i.e., Os, Ir, Ru) and Rh would partition into the early-formed *mss* leaving a Cu-rich residual liquid enriched in Pt and Pd. In contrast, our observations suggest that in the Caridad chromite deposit the precursor *mss* concentrated most of the PGE leaving behind a Cu-rich residual liquid depleted Pt and Pd. Interestingly, the experiments by Peregoedova et al. (2004) showed that *mss* can concentrate significant amounts of Pt, Ir and Pd in solid-solution at high temperatures (at least 0.2 wt.%). Available LA-ICP-MS data from *mss* (regardless of its Ni- or Fe-rich composition) hosted in mantle peridotite indicate support these experimental results indicating that *mss* can effecitly concentrate both IPGE and PPGE (i.e., Pt, Pd, Rh) in solid solution at high temperatures (e.g., Wang et al. 2009; González-Jiménez et al. 2014; Saunders et al. 2015; Tassara et al. 2017). In the Caridad chromite deposit, as temperature decreased to around 610 °C, the metal excess in the precursor PGE-rich *mss* would have been exsolved to PGE-rich pentlandite (Fig. 7a-b). With decreasing temperature, the ability of the structure of pentlandite to retain Ir and Pt as solid solution also decreases (Makovicky et al. 1986, 1988, 1990). This structural re-arrangement promoted the formation of a discrete Ir-Pt-(Os-Cu) domains as observed in Figures 2a and b. However, and as noted above, the PGE content was not high enough to result in a complete structural ordering and exsolution of PGE lamellae, such as e.g., Rh-rich lamella observed in Rh-rich pentlandite from the Bushveld Complex (Junge et al. 2015).

On the other hand, the Cu-rich melt that coexisted with the *mss* at approximately 1000 °C should have still contained appreciable amounts of Ni (Fig. 9a-b). This PGE-depleted sulfide liquid was very likely the parental melt for the assemblage of PGE-poor pentlandite ± millerite ± pyrite ± chalcopyrite coexisting with Ru-rich pentlandite shown in Figures 2a and b. This interpretation is consistent with experimental data and observations in natural samples showing that when pentlandite forms early from a PGE-rich *mss*, it inherits most of the PGE whereas coexisting millerite, pyrite and chalcopyrite concentrates little or no PGE (Piña et al. 2012 and references therein). In this model, the exsolution-induced formation of discrete Ir-Pt alloy must have occurred soon after the formation of pentlandite but

448 before millerite, as shown by the structural relationship between Ir-Pt domain and
449 millerite (Fig. 6).

450 Figure 2c-d shows a very different scenario. In this composite grain made up
451 of millerite associated with Ru-rich pentlandite (with up to 8.67 wt.% Ru and 3.53
452 wt.% Os) there are two types of nanoparticles of Ir-Pt. Nanometer sized (<250 nm)
453 particles with a preferred crystallographic orientation, and a larger single fibrous grain
454 ~2 μm across. Unlike the scenario discussed before, the relatively high PGE content
455 of this pentlandite matrix may have favored the formation of discrete and oriented
456 PGE-bearing lamellae, as a result of the low-temperature exsolution. In contrast, the
457 fibrous texture of the larger Ir-Pt particles may reflect the coalescence of several sub-
458 microscopic particles of these noble metals. The coarsening of Ir-Pt particles is
459 expected to occur with an increase in temperature favoring diffusion and growth by
460 Ostwald ripening (e.g., Reich et al. 2006; González-Jiménez et al. 2015) and not upon
461 cooling when the efficiency of diffusional processes are dramatically decreased,
462 particularly below 300 °C (Brenan et al., 2000; Fonseca et al. 2017). Thus, it is very
463 likely that Ir-Pt particles were segregated during the crystallization of chromite (e.g.,
464 Finnigan et al. 2008) and later entrained by sulfide droplets once sulfide saturation
465 was achieved in the basaltic melt, similar to observations in other natural samples and
466 experiments (e.g., Tredoux et al., 1995; Ballhaus and Sylvester, 2000; Wirth et al.
467 2013; Laurenz et al. 2013; Helmy et al. 2013). The formation of the Ir-Pt
468 nanoparticles is expected in the silicate melt due the strong tendency of these two
469 metals to form nuggets in high temperature silicate melts (~ 1500-1200 °C; Amossé et
470 al. 1991; Borisov and Palme 1995, 1997). The results of the experiments carried out
471 by Borisov and Palme (1997) indicate that once suspended in the silicate liquid, Ir and
472 and Pt will rapidly react to form Ir-Pt alloys owing their higher alloy/sulfide partition
473 coefficient than the other PGE (Peregoedova et al. 2004; Fonseca et al. 2017). This
474 siderophile behavior is strongly reinforced when chromite crystallizes from the melt,
475 as the stability of pure Ir and Pt are strongly dependent of f_{O_2}changes in the silicate
476 melt, induced by chromite crystallization (Mungall 2005; Matveev and Ballhaus
477 2002; Bockrath et al. 2004). The results of Finnigan et al. (2008) confirm this
478 observation where Ir-Pt nanocrystals (~ 700 nm in diameter) were crystallized directly
479 from basaltic melt at the P-T-f_{O_2} conditions relevant for the formation of chromite

deposits in the upper mantle, i.e., 0.5 GPa, T ~ 1300-1400 °C and f_{O_2} at FMQ. Under these conditions, sub-micrometric Ir-Pt particles might have been suspended in the silicate melt or attached to growing chromite crystals as metallic, oxygen or sulfur-bearing compounds (Wirth et al. 2013). If these Ir-Pt nanoparticles were originally captured by the sulfide melt, as soon as the *mss* crystallized they should have been adhered to the solid phase due to their wetting properties. Aggregation and coalescence of these nanoparticles would produce larger Ir-Pt nanocrystals that might growth to micrometric-sized Ir-Pt (e.g., Fig. 2c-d; Fonseca et al. 2017). Therefore, the occurrence of Ir-Pt oriented nanoparticles in the Ru-rich pentlandite would reflect the preferential clustering of these particles along growth planes in pentlandite (Wirth et al. 2013; Junge et al. 2015). This interpretation points to the fact that PGE fractionation is not exclusively dependent on the sulfide-silicate or *mss*/sulfide liquid partition, but may be also influenced by other factors including physical separation and collection of previously crystallized nanoalloys (Ballhaus et al. 2006; Helmy et al. 2013; Wirth et al. 2013; Junge et al. 2015).

Implications for PGE concentration in ore deposits

The micro-to-nano scale investigation of PGE-rich BMS from the Caridad deposit in the Mayarí-Baracoa Ophiolite, eastern Cuba provides new insights into PGE partitioning during the formation of chromite ores in the mantle. Our observations link the formation of Ir-Pt nanoparticles with the crystallization of BMS, an occurrence that was not previously described in mantle-derived peridotites, or in ore deposits. At the Caridad chromite deposit the formation of Ir-Pt nanoparticles and nanodomains is attributed to two different processes: (1) exsolution of PGE from pentlandite during cooling (~610 °C), and (2) physical fractionation of Ir-Pt nanoparticles form a silicate melt, followed by entrainment into a sulfide melt. These observations suggest that, if noble metal nanoparticles can indeed precipitate from a silicate melt, the PGE content of a given sulfide assemblage may be significantly influenced by the physical incorporation of the nanoparticles into particular sulfides. Therefore, we suggest that the partitioning behavior of PGE, while predominantly controlled by equilibrium thermodynamics (i.e., partition coefficients), may be at least partly influenced by non-equilibrium kinetic and nanoscale effects (i.e., incorporation of metal nanoclusters). The mineralogical evidence provided in this paper, in addition

to experiment observation of noble metal nanonuggets in silicate melts (e.g., Ballhaus et al., 2006 and Anenburg and Mavrogenes, 2016), highlight the importance of studying of solid inclusions in chromite ores to better understand the mechanism of fractionation of noble metals in magmatic systems.

ACKNOWLEDGEMENTS

This research was financially supported by FEDER Funds through the projects CGL2015-65824-P and CGL2014-55949-R granted by the Spanish "Ministerio de Economía y Competitividad". Additional funding was provided by the Millennium Science Initiative (MSI) grant "Millennium Nucleus for Metal Tracing along Subduction" (NC130065, Ministry of Economy, Chile). JMGJ acknowledges financial support of the Ramón y Cajal Fellowship RYC-2015-17596 granted by the Spanish MINECO.

REFERENCES

Ahmed, A.H., and Arai, S., 2003. Platinum-group minerals in podiform chromitites of the Oman ophiolite. Canadian Mineralogist 41, 597–616.

Amossé J, Allibert M, Fischer W, and Piboule M (1990) Experimental study of the solubility of platinum and iridium in mafic silicate melts. Implications for the differentiation of platinum-group elements during magmatic processes. Chemical Geology 81, 45-53.

Anenburg, M., Mavrogenes, J.A. 2016) Experimental observations on noble metal nanonuggets and Fe-Ti oxides, and the transport of platinum group elements in silicate melts. Geochimica et Cosmochimica Acta (2016), doi: http://dx.doi.org/10.1016/j.gca.2016.08.010.

Armstrong J.T. (1988) Quantitative analysis of silicates and oxide minerals: Comparison of Monte-Carlo, ZAF and Phi-Rho-Z procedures. Microbeam Analysis, 239-246.

Ballhaus, C. (1998) Origin of podiform chromite deposits by magma mingling. Earth and Planetary Science Letters 156, 185–193.

Ballhaus, C., Syslvester, P. (2000) Noble Metal Enrichment Processes in the Merensky Reef, Bushveld Complex. Journal of Petrology, 545–561,

Ballhaus, C., Tredoux, M., Späth, A. (2001) Phase relations in the Fe-Ni-Cu-PGE-S system at magmatic temperature and application to massive sulfide ores of the Sudbury igneous complex.

Ballhaus, C., Bockrath, C., Wohlgemuth-Ueberwasser, C., Laurenz, V., and Berndt, J. (2006) Fractionation of the noble metals by physical processes. Contributions to Mineralogy and Petrology 152, 667–684.

Ballhaus, C., Tredoux, M., and Spaeth, A. (2001) Phase relations in the Fe–Ni–Cu–PGE–S system at magmatic temperature and application to massive sulphide ores of the Sudbury igneous complex. Journal of Petrology 42 (10), 1911–1926.

549 Barnes, S.J., Ripley E.M. (2016) Highly Siderophile and Strongly Chalcophile Elements in
550 Magmatic Ore Deposits. Reviews in Mineralogy and Geochemistry 81, 725-774.

551 Bockrath, C., Ballhaus, C., and Holzheid, A. (2004) Stabilities of laurite RuS_2 and
552 monosulphide liquid solution at magmatic temperature. Chemical Geology 208, 265–
553 271.

554 Borisov, A., and Palme, H. (1995) The solubility of iridium in silicate melts: New data from
555 experiments with $Ir_{10}Pt_{90}$ alloys. Geochimica et Cosmochimica Acta 59, 481-485.

556 Borisov, A., and Palme, H. (1997) Experimental determination of solubility of platinum in
557 silicate melts. Geochimica et Cosmochimica Acta 61, 4349-4347.

558 Brenan, J.M., Cherniak, D.J., and Rose, L.A. (2000) Diffusion of osmium in pyrrhotite and
559 pyrite; implications for closure of the Re–Os isotopic system. Earth and Planetary
560 Science Letters 180 (3–4), 399–413.

561 Chang, Y. A., and Hsieh, K-C. (1986) Thermochemical description of the ternary iron nickel-
562 sulphur system. In Nickel Metallurgy: volume 1: Extraction and Refining of Nickel, E.
563 Ozberk and S.W. Marcuson, eds., Proceedings of the 25th annual conference of
564 metallurgists, Canadian Institute of Mining and Metallurgy, p.248-277.

565 Cabri, L.J. 1973. New data on phase relations in the Cu-Fe-S system. Economic Geology 64,
566 443-454.

567 Craig, J.R. and Kullerud, G. (1969) Phase Relations in the Cu-Fe-Ni-S System and Their
568 Application to Magmatic Ore Deposits, Economic Geology 4, 344–358.

569 Craig, J.R. (1973) Pyrite-pentlandite assemblages and other low temperature relations in the
570 Fe-Ni-S system. Americal Journal of Science, Cooper vol. 273-A, 496-510.

571 Donovan J.J., Snyder D.A. and Rivers M.L. (1993) An Improved Interference Correction for
572 Trace Element Analysis. Microbeam Analysis, 2: 23-28.

573 Donovan J.J. and Tingle T.N. (1996) An Improved Mean Atomic Number Correction for
574 Quantitative Microanalysis. Journal of Microscopy, 2, 1-7.

575 Donovan J.J., Singer and Armstrong J.T. (2016) A New EPMA Method for Fast Trace
576 Element Analysis in Simple Matrices, American Mineralogist, 101, 1839-1853.

577 Ebel, D.S., Naldrett, A.J. (1996) Fractional crystallization of sulfide ore liquids at high
578 temperature. Economic Geology 91, 607–621.

579 Fedorova, Zh.N., and Sinyakova, E.F. (1993) Experimental investigation of physicochemical
580 conditions of pentlandite formation. Russian Journal of Geology and Geophysics 34,
581 79– 87.

582 Finnigan, C.S., Brenan, J.M., Mungall, J.E., McDonough, W.F., 2008. Experiments and
583 models bearing on the role of chromite as a collector of platinum group minerals by
584 local reduction. Journal of Petrology 49, 1647–1665.

585 Fleet, M. E., and Pan, Y., 1994, Fractional crystallization of anhydrous sulfide liquid in the
586 system Fe-Ni-Cu-S, with application to magmatic sulfide deposits. Geochimica et
587 Cosmochimica Acta 58, 3369-3377.

588 Fleet, M.E. (2006) Phase equilibria at high temperatures. Reviews in Mineralogy and
589 Geochemistry 61, 365-419.

590 Fleet, M.E., Crocket, J.H., Menghua, L., Stone, W.E. (1999) Laboratory partitioning of
591 platinum-group elements (PGE) and gold with application to magmatic sulfide–PGE
592 deposits. Lithos 47, 127-142.

593 Fonseca, R.O.C., Brückel, K., Bragagni, A., Litzke, F., Speelmanns, I.M., Wingwright, A.N.
594 (2017) Fractionation of Rhenium from Osmium during noble metal alloy formation in

association with sulfides: Implications for the interpretation of model ages in alloy-bearing magmatic rocks. Geochimica et Cosmochimica Acta, http://dx.doi.org/10.1016/j.gca.2017.04.041

Garuti, G., Zaccarini, F., and Economou-Eliopoulos, M. (1999) Paragenesis and composition of laurite from chromitites of Othrys (Greece): implications for Os–Ru fractionation in ophiolitic upper mantle of the Balkan Peninsula. Mineralium Deposita 34, 312–319.

Gervilla, F., Proenza, J.A., Frei, R., González-Jiménez, J.M., Garrido, C.J., Melgarejo, J.C., Meibom, A., Díaz-Martínez, R., and Lavaut, W. (2005) Distribution of platinum-group elements and Os isotopes in chromite ores from Mayarí-Baracoa Ophiolitic Belt (eastern Cuba). Contributions to Mineralogy and Petrology 150, 589–607.

González-Jiménez, J.M., Proenza, J.A., Gervilla, F., Melgarejo, J.C., Blanco-Moreno, J.A., Ruiz-Sánchez, R., and Griffin, W.L. (2011) High-Cr and high-Al chromitites from the Sagua de Tánamo district, Mayarí-Cristal Ophiolitic Massif (eastern Cuba): constraints on their origin from mineralogy and geochemistry of chromian spinel and platinum-group elements. Lithos 125, 101–121.

González-Jiménez, J.M., Gervilla, F., Griffin, W.L., Proenza, J.A., Augé, T., O'Reilly, S.Y., and Pearson, N.J. (2012) Os-isotope variability within sulfides from podiform chromitites. Chemical Geology 291, 224–235.

González-Jiménez, J.M., Villaseca, C., Griffin, W.L., O'Reilly, S.Y., Belousova, E., Ancochea, E., Pearson, N.J. (2014) Significance of ancient sulfide PGE and Re–Os signatures in the mantle beneath Calatrava, Central Spain. Contributions to Mineralogy and Petrology 168, 1047, https://doi.org/10.1007/s00410-014-1047-x.

González-Jiménez, J. M., and Reich, M. (2017) An overview of the platinum-group element nanoparticles in mantle-hosted chromite deposits. Ore Geology Reviews 81, 1236-1248.

Helmy, H.M., Ballhaus, C., Fonseca, R.O.C., Wirth, R., Nagel, T., and Tredoux, M. (2013) Noble metal nanoclusters and nanoparticles precede mineral formation in magmatic sulphide melts. Nature Communications http://dx.doi.org/10.1038/ncomms3405.

Hill, R., and Roeder, P. (1974) The crystallization of spinel from basaltic liquids as a function of oxygen fugacity. Journal of Geology 82, 709–729.

Holwell, D.A., Keays, R.R.,McDonald, I., and Williams, M.R. (2015) Extreme enrichment of Se, Te, PGE and Au in Cu sulfide microdroplets: evidence from LA-ICP-MS analysis of sulphides in the Skaergaard Intrusion, east Greenland. Contributions to Mineralogy and Petrology 170 (53).

Jugo, P.J., 2009. Sulfur content at sulfide saturation in oxidized magmas. Geology 37, 415-418.

Junge, M., Wirth, R., Oberthür, R., Melcher, F., and Schreiber, A. (2015) Mineralogical siting of platinum-group elements in pentlandite from the Bushveld Complex. South Africa. http://dx.doi.org/10.1007/s00126-014-0561-0.

Kitakaze, A., Machida, T., and Komatsu, R. (2016) Phase relations in the Fe-Ni-S system from 875 to 650 ºC. The Canadian Mineralogist 54, 1175-1186.

Kogiso, T., Suzuki, K., Suzuki, T., and Uesugi, K., 2008. Two- and three-dimensional imaging of platinum-group minerals at submicrometer scale with synchrotron X-ray. Goldschmidt Conference Abstracts 2008, p. 1212 (www.minersoc.org).

Kullerud, G. (1962) Two-liquid fi eld in the Fe-S system. Carnegie Inst Wash, Year Book 60, 174-176.

Kullerud, G. (1963) Thermal stability of pentlandite. The Canadian Mineralogist 7, 353-366

642 Kullerud G, and Yund RA (1962) The Ni-S system and related minerals. Journal of Petrology
643 3, 126-175.

644 Laurenz, V., Fonseca, R.O., Ballhaus, C., Jochum, K.P., Heuser, A., and Sylvester, P.J., 2013.
645 The solubility of palladium and ruthenium in picritic melts: 2. The effect of sulfur.
646 Geochimica et Cosmochimica Acta 108, 172–183.

647 Li, C., Barnes, S.-J., Makovicky, E., Rose-Hansen, J., Makovicky, M., 1996. Partitioning of
648 nickel, copper, iridium, rhodium, platinum, and palladium between monosulfide solid
649 solution and sulfide liquid: effects of composition and temperature. Geochimica et
650 Cosmochimica Acta 60, 1231–1238.

651 Lorand, J.-P., Alard, O., and Luguet, A., 2010. Platinum-group element micronuggets and
652 refertilization process in Lherz orogenic peridotite (northeastern Pyrenees, France).
653 Earth and Planettary Science Letters 289, 298–310.

654 Luguet, A., and Reisberg, L. (2016) Highly Siderophile Element and ^{187}Os Signatures in
655 Non-cratonic Basalt-hosted Peridotite Xenoliths: Unravelling the Origin and Evolution
656 of the Post-Archean Lithospheric Mantle. Reviews in Mineralogy and Geochemistry
657 81, 305-367.

658 Makovicky, M., Makovicky, E., and Rose-hansen, J. (1986) Experimental studies on the
659 solubility and distribution of platinum-group elements in base-metal sulphides in
660 platinum deposits. In: Gallagher, M.J., Ixer, R.A., Neary, C.R., Prichard, H.M. (Eds.),
661 Metallogeny of Basic and Ultrabasic Rocks. The Institution of Mining and Metallurgy,
662 London, U.K, pp. 415–425.

663 Makovicky, M., Makovicky, E., and Rose-Hansen, J. (1988) Experimental evidence of the
664 formation and mineralogy of platinum and palladium ore deposits. In: Boissonnas, J.,
665 Omenetto, P. (Eds.), Mineral Deposits within the European Community. Springer-
666 Verlag, Berlin, Germany, pp. 303–317.

667 Makovicky, E., Karup-Møller, S., Makovicky, M., and Rose-Hansen, J. (1990) Experimental
668 studies on the phase systems Fe–Ni–Pd–S and Fe–Pt–Pd–As–S applied to PGE
669 deposits. Mineralogy and Petrology 42, 307–319.

670 Malitch, K.N., Melcher, F., Mühlhans, H., 2001. Palladium and gold mineralization in
671 podiform chromitite at Kraubath, Austria. Mineralogy and Petrology 73, 247–277.

672 Marchesi, C., Garrido, C.J., Godard, M., Proenza, J.A., Gervilla, F., and Blanco-Moreno, J.
673 (2006) Petrogenesis of highly depleted peridotites and gabbroic rocks from the Mayarí-
674 Baracoa Ophiolitic Belt (eastern Cuba). Contributions to Mineralogy and Petrology
675 151, 717–736.

676 Marchesi, C., Garrido, C.J., Boch, D., Proenza, J.A., Gervilla, F., Monié, P., and Rodríguez-
677 Vega, A. (2007) Geochemistry of Cretaceous magmatism in eastern Cuba: recycling of
678 North American continental sediments and implications for Subduction Polarity in the
679 Greater Antilles Paleo-Arc. Journal of Petrology 48, 1813–1840.

680 Marchesi, G., González-Jiménez, J.M., Gervilla, F., Garrido, C.J., Griffin, W.L., O'Reilly,
681 S.Y., Proenza, J.A., and Pearson, N.J. (2011) In situ Re-Os isotopic analysis of
682 platinum-groupminerals from the Mayarí-Cristal ophiolitic massif (Mayarí-Baracoa
683 Ophiolitic Belt, eastern Cuba): implications for the origin of Os-isotope heterogeneities
684 in podiform chromitites. Contributions to Mineralogy and Petrology 161, 977–990.

685 Matveev, S., and Ballhaus, C. (2002) Role of water in the origin of podiform chromitite
686 deposits. Earth and Planettary Science Letters 203, 235–243.

687 Melcher, F., Grum,W., Simon, G., Thalhammer, T. V. and Stumpfl, E. F. (1997) Petrogenesis
688 of the ophiolitic giant chromite deposits of Kempirsai, Kazkhstan: a study of solid and
689 fluid inclusions in chromite. J. Petrol 38, 1419–1458.

690 Misra, K.C., and Fleet, M.E. (1973) The chemical compositions of synthetic and natural
691 pentlandite assemblages. Economic Geology 68, 518-539.

692 Mungall, J.E. (2005) Magmatic geochemistry of the platinum-group elements. In: Mungall.,
693 J.E. (Ed.), Exploration from Platinum-Group Elements Deposits: Short Course Series -
694 Mineralogical Association of Canada, vol. 35, pp. 1–34.

695 Mungall, J.E., Andrews, D.R.A., Cabri, L.J., Sylvester, P.J., Tubrett, M (2005) Partitioning of
696 Cu, Ni, Au, and platinum-group elements between monosulfide solid solution and
697 sulfide melt under oxygen and sulfur fugacities. Geochimica et Cosmochimica Acta 69,
698 4349-4360.

699 Naldrett, A.J., Lehmann, J., and Augé, T. (1989) Spinel non-stoichiometry and reactions
700 between chromite and closely associated sulphides, with examples from ophiolite
701 complexes. In: Predergast, M.D., Jones, J. (Eds.), Magmatic sulphides-the Zimbabwe
702 volume. The Institution of Mining and Metallurgy, London, pp. 221–227.

703 Naldrett, A.J., Kinnaird, J., Wilson, A., Yudovskaya, M., McQuade, S., Chunnett, G., and
704 Stanley, C. (2009) Chromite composition and PGE content of Buhsveld chromitites:
705 Part 1 - the lower and middle groups. Applied Earth Science (Trans. Inst. Min. Metall.
706 B) 118, 131-161.

707 Pearson, N.J., Alard, O., Griffin, W.L., Jackson, S.E., O'Reilly, S.Y. (2002) In situ
708 measurement of Re–Os isotopes in mantle sulfides by laser ablation multicollector-
709 inductively coupled plasma mass spectrometry: analytical methods and preliminary
710 results. Geochimica et Cosmochimica Acta 66, 1037–1050.

711 Peregoedova, A.V., Barnes, S.J., and Baker, D.R. (2004) The formation of Pt–Ir alloys and
712 Cu–Pd-rich sulfide melts by partial desulfurization of Fe–Ni–Cu sulfides: results of
713 experiments and implications for natural systems. Chemical Geology 208, 247–264.

714 Piña, R., Gervilla, F., Barnes, S.J., Ortega, L., Lunar, R. (2012) Distribution of platinum-
715 group and chalcophile elements in the Aguablanca Ni–Cu sulfide deposit (SW Spain):
716 Evidence from a LA-ICP-MS study. Chemical Geology 302-303, 61-75.

717 Piña, R., Gervilla, F., Barnes, S.J., Oberthür, T., Lunar, R. (2016) Platinum-group elment
718 concentration in pyrite from the Main Sulfide Zone of the Great Dyne of Zimbabwe.
719 Mineralium Deposita 51, 853-872.

720 Proenza, J.A., Gervilla, F., Melgarejo, J.C., Bodinier, J.L., 1999. Al- and Cr-rich chromitites
721 from the Mayarí-Baracoa Ophiolitic Belt (eastern Cuba): consequence of interaction
722 between volatile-rich melts and peridotite in suprasubduction mantle. Economic
723 Geology 94, 547–566.

724 Proenza, J.A., Alfonso, P., Melgarejo, J.C., Gervilla, F., Tritlla, J., Fallick, A.E., 2003. D, O
725 andC isotopes in podiform chromitites as fluid tracers for hydrothermal alteration
726 processes of the Mayarí-Baracoa Ophiolitic Belt, eastern Cuba. Journal of Geochemical
727 Exploration 78–79, 1–6.

728 Proenza, J.A., Díaz-Martínez, R., Iriondo, A., Marchesi, C., Melgarejo, J.C., Gervilla, F.,
729 Garrido, C.J., Rodríguez-Vega, A., Lozano-Santacruz, R., Blanco-Moreno, J.A., 2006.
730 Primitive island-arc Cretaceous volcanic rocks in eastern Cuba: the Téneme Formation.
731 Geologica Acta 4, 103–121.

732 Reich, M., Utsunomiya, S., Kesler, S.E., Wang, L.M., Ewing, R.C., Becker, U., 2006.
733 Thermal behavior of metal nanoparticles in geologic materials. Geology 34, 1033–
734 1036.

735 Saunders, J.E., Pearson, N.J., O'Reilly, S.Y., Griffin, W.L. (2015) Sulfide metasomatism and
736 the mobility of gold in the lithospheric mantle. Chemical Geology 410, 149-161.

737 Shewman, R.W., Clark, L.A. (1970) Pentlandite phase relations in the Fe-Ni-S system and

notes on the monosulfide solid solution. Canian Journal of Earth Science 7, 67-85.

Sugaki, A., and Kitakaze, A. (1998) High form of pentlandite and its thermal stability. American Mineralogist 83, 133-140.

Tassara, C.S. González-Jiménez, J.M., Reich, M., Schilling, M., Morata, D., Begg, G., Saunders, J. E., Griffin, W.L., O'Reilly, S.Y., Gregoire, M., Barra, F., Corgne, A. (2017) Plume-subduction interaction forms large auriferous provinces. Nature Communications 8, 10.1038/s41467-017-00821-z.

Tolstykh, N.D., Foley, J.Y, Sidorov, E.G., Laajoki, K.V.O. (2002) Composition of the platinum-group minerals in the Salmon River placer deposit, Goodnews Bay, Alaska. Canadian Mineralogist 40, 463-471.

Tredoux, M., Lindsay, N.M., Davies, G. and McDonald I. (1995) The fractionation of platinum-group elements in magmatic systems with the suggestion of a noval causal mechanism. South African Journal of Geology 98, 157-167.

Turchi, P.E.A., Drchal, V., and Kudronsvsky, J. (2006) Stability and ordering properties of fcc alloys based on Rh, Ir, Pd and Pt. Physical Review B 74, 064202.

Wang, K.L., O'Reilly, S.Y., Griffin, W.L., Pearson, N.J., Zhang, M. (2009) Sulfides in mantle peridotites from Penghu Island, Taiwan: melt percolation, PGE fractionation, and the lithospheric evolution of the South China block. Geochimica Cosmochimica Acta 73, 4531–4557.

Wirth, R., Reid, D., and Schreiber, A. (2013) Nanometer-sized platinum-group minerals (PGM) in base metal sulfides: new evidence for an orthomagmatic origin of the Merensky reef PGE ore deposit. Bushveld Complex. South Africa. Can. Mineral. 51, 143–155.

Wood, S .A. (1987) Thermodynamic calculations of the volatility of the platinum group elements (PGE): the PGE content of fluids at magmatic temperatures. Geochimica et Cosmochimica Acta 61, 3041-3050.

FIGURE CAPTION

Figure 1. Location of the Caridad chromitite in the northern part of the Mayarí-Cristal Massif and simplified geological map of the area (modified from González-Jiménez et al., 2012).

Figure 2. Backscattered electron images base-metal sulfides hosted within unaltered chromite grains from the Caridad chromite deposit in Cuba. Ir-Pt nanoparticles are also shown. Mill: millerite; Pn: pentlandite; Cp: chalcopyrite; Py: pyrite; Ru-Pn: Ru-rich pentlandite.

Figure 3. Wavelength-dispersive spectrometry (WDS) X-ray elemental maps of base-metal sulfide assemblages. (**a-f**) and (**g-l**) show the solid composite inclusions in Figures 1a and 1b, respectively. Color scale bars show element concentrations in wt.%; mdl: minimum detection limit. Single-spot EPMA analyses of this grain correspond to those named as CAR-1-B1 a to w provided in Table S1.

779 **Figure 4.** Chemical composition of the base-metal sulfides in terms of Ni, Fe and S
780 (**a-b**) and PGE (**c-f**). Note that in Figures **c-f** each bar shown in the histogram
781 represents a single EPMA spot analysis.
782 **Figure 5.** Representative time-resolved LA-MC-ICP-MS spectra collected during Re-
783 Os analysis of Ru-rich pentlandite (González-Jiménez et al. 2012). The transient
784 spectrum of ^{194}Pt shows a peak that is interpreted as a Pt-bearing inclusion.
785 Despite that Pt-dominated inclusions associated with Caridad sulphides contain
786 Ir, the isotopes of this element did not change in the time-resolve spectra
787 because and monitoring Ir-bearing solution was introduced during ablation (see
788 Pearson et al., 2002).
789 **Figure 6.** TEM images of Ru-rich pentlandite, millerite and Ir-Pt nanoparticle (grain
790 shown in Figures 1a and 2a-f). (**a**) HAADF-STEM image shows a triangular Ir-
791 Pt nanoparticle in contact with Ru-rich pentlandite and millerite. The EDS maps
792 on the right-hand side show the chemical composition of the selected area in (a)
793 indicating: (i) relative enrichment and homogeneous distribution of Ru and Co
794 in Ru-rich pentlandite and the Ir-Pt nano particle, with respect to millerite; (ii)
795 correspondence between Fe, Ir, Pt, Cu, and Os in the Ir-Pt nanoparticle; and (iii)
796 relative depletion in Ni in the Ir-Pt nanoparticle with respect to millerite and
797 pentlandite. (**b**) Low-magnification BFTEM image of sharp grain boundaries
798 between Ir-Pt, and millerite (dashed line), and diffused grain boundary between
799 Ir-Pt and Ru-rich pentlandite (grey thick line). (**c**) HRTEM image of a single Ir-
800 Pt domain, with its associated diffraction pattern obtained by Fast Fourier
801 Transformation (FFT). (**d**) HRTEM image of the grain boundary area between
802 the Ir-Pt domain and the Ru-pentlandite matrix, and its FFT diffraction pattern.
803 Both domains show the same diffraction pattern. (**e**) HRTEM image showing
804 the continuous boundary between Ir-Pt domain and millerite. Insets show the
805 FFT images of the Ir-Pt nanoparticle, the millerite matrix and the interface
806 between the two.
807 **Figure 7.** Phase relations (1 bar) in the Fe-Ni-S system at 1000 °C (**a**), 550 °C (**b**),
808 250 °C (**c**) and 135-100 °C (**d**). The plots were modified from Kullerund and
809 Yund (1969), Craig (1973) and Naldrett et al. (2009). Keys: *mss*: monosulfide
810 solid solution [$(Fe,Ni)_{1-x}S$], vs: vaesite [NiS_2], Po(m): monoclinic pyrrothite
811 [$Fe_{1-X}S$], Po(h): hexagonal pyrrhotite [$Fe_{1-x}S$)], Tr: troilite [FeS], py: pyrite

812 [FeS_2], pn: pentlandite [$(Ni,Fe)_9S_8$)], vio: violarite [$FeNi_2S_4$], mill: millerite
813 [NiS], godlevskite [Ni_7S_6], hz: heazlewoodite [Ni_3S_2]. At 100 °C *mss* already
814 coexists with Ni-Fe liquid (**a**) whereas at 550 °C pentlandite (purple star-1)
815 derived from the subsolidus recrystallization of the *mss* at 610 °C is present. (**b**)
816 Arrows in the dotted red line indicate the possible pathway of progressive
817 enrichment in Ni of *mss* upon cooling, as a result of Fe exchange between the
818 base-metal sulfide inclusion and the larger chromite host (e.g., Naldrett et al.,
819 1989). In this plot, the red dots indicate all possible compositions of *mss* in
820 equilibrium with pentlandite at the given temperature. At temperatures below
821 300 °C, *mss* decomposes into a variety of 2- and 3-phase assemblages. Millerite
822 (purple star-2) is stable with pentlandite at 250 °C (**c**), while complete
823 equilibrium of composite assemblages of millerite + pentlandite + pyrite (purple
824 star-3), as those shown in Figure 2b are only stable at much lower temperatures
825 (135-100 °C) (**d**).

826 **Figure 8.** Phase relations (1 bar) in Fe-Ni-S space (**a** and **c**) and T vs. f_{S_2} space **(b)**.
827 The ternary diagram in **(a)** and **(c)** show phase relations at 900 °C and 850 °C,
828 respectively (Kullerud and Yund, 1969; Kitakaze et al., 2016), while the binary
829 plot in (**b**) is from Melcher et al. (1997). Keys: *mss*: monosulfide solid solution
830 [$(Fe,Ni)_{1-x}S$], vs: vaesite [NiS_2], pn(h): high-temperature form of pentlandite
831 [$(Ni,Fe)_9S_8$)]. In **(a),** a high-temperature form of millerite (α-NiS) can be
832 produced by Fe loss of the *mss* (purple star-1), which at much lower
833 temperature (~ 379 °C) inverts to low-temperature millerite (β-NiS). The excess
834 Fe incorporated high temperature in millerite is exsolved as blebby pyrite
835 during the polymorphic change (e.g., Fig. 2g). The sections in **(b)** and **(c)** were
836 chosen to illustrate the crystallization of millerite (with or without pyrite) and
837 pentlandite from melts at high temperature, and not as a result of subsolidus
838 recrystallization of a precursor *mss*. In **(b)**, it is shown that α-NiS can
839 crystallize at the solidus temperatures of chromite (1000-1200 °C; grey field)
840 whereas in **(c)** the high-temperature form of pentlandite may have been formed
841 directly from a melt or by reaction of millerite with a sulfide liquid (purple star-
842 2).

843 **Figure 9.** Phase relations (1 bar) in the sulfur-rich portion of the Cu-Fe-Ni-S system
844 at 1000 °C (**a**), 850 °C (**b**) (Craig and Kullerud, 1969; Cabri, 1973). Keys: *mss*:

monosulfide solid solution [$(Fe,Ni)_{1-x}S$], vs: vaesite [NiS_2], bn ss: bornite solid solution [$CuFe_2S_4$], cp ss: chalcopyrite solid solution [$CuFeS_2$]. Note that in **(a),** the *mss* (purple star-1) coexists with two liquids at 1000 °C (a Ni-Fe-rich liquid in the Ni-Fe-S portion and a Cu-rich liquid in the Cu-Fe-S portion). At 850°C, the *mss* coexists with chalcopyrite (purple star-2), as indicated by the dotted red line.

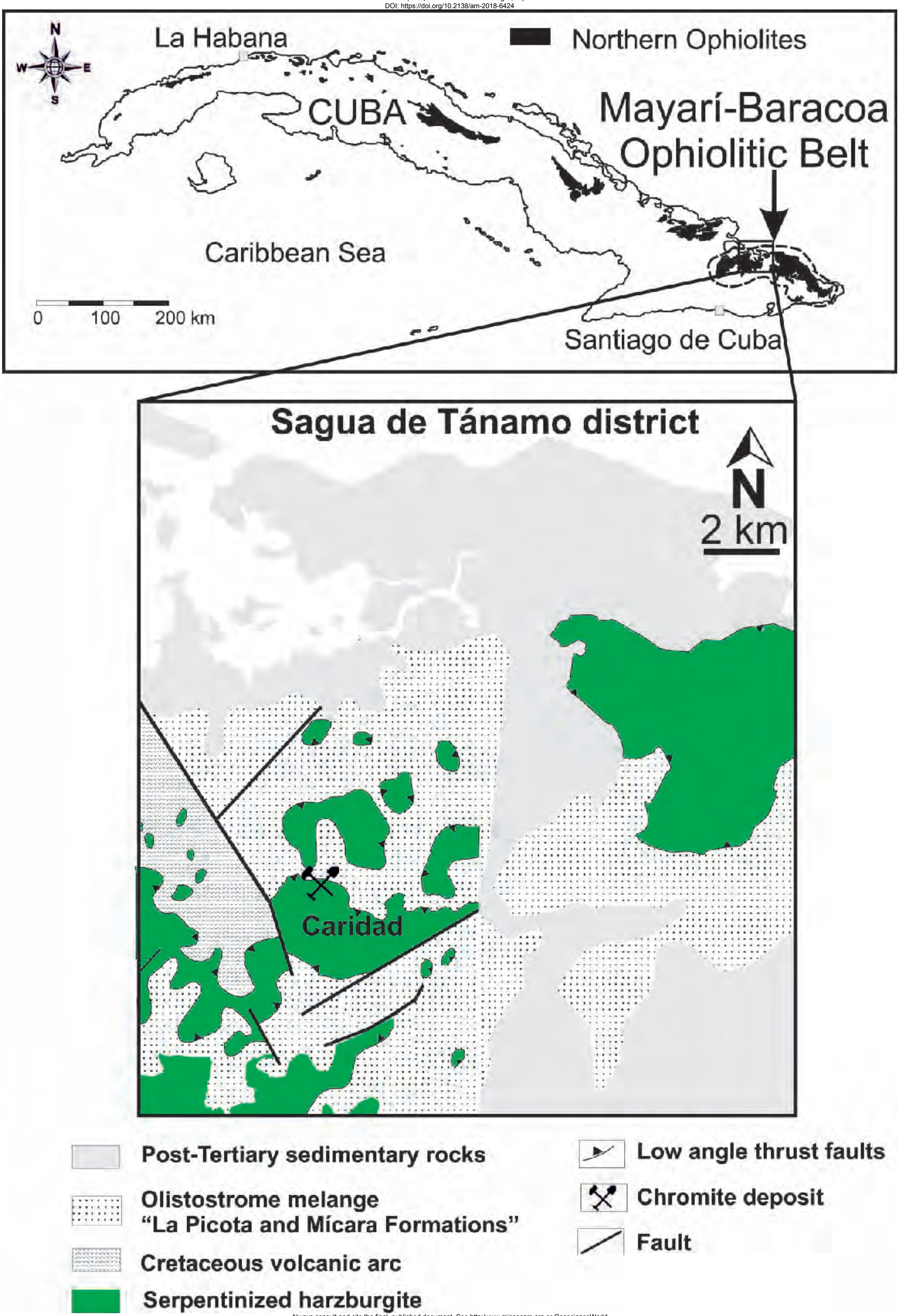

This is a preprint, the final version is subject to change, of the American Mineralogist (MSA)
Cite as Authors (Year) Title. American Mineralogist, in press.
DOI: https://doi.org/10.2138/am-2018-6424

Figure 2

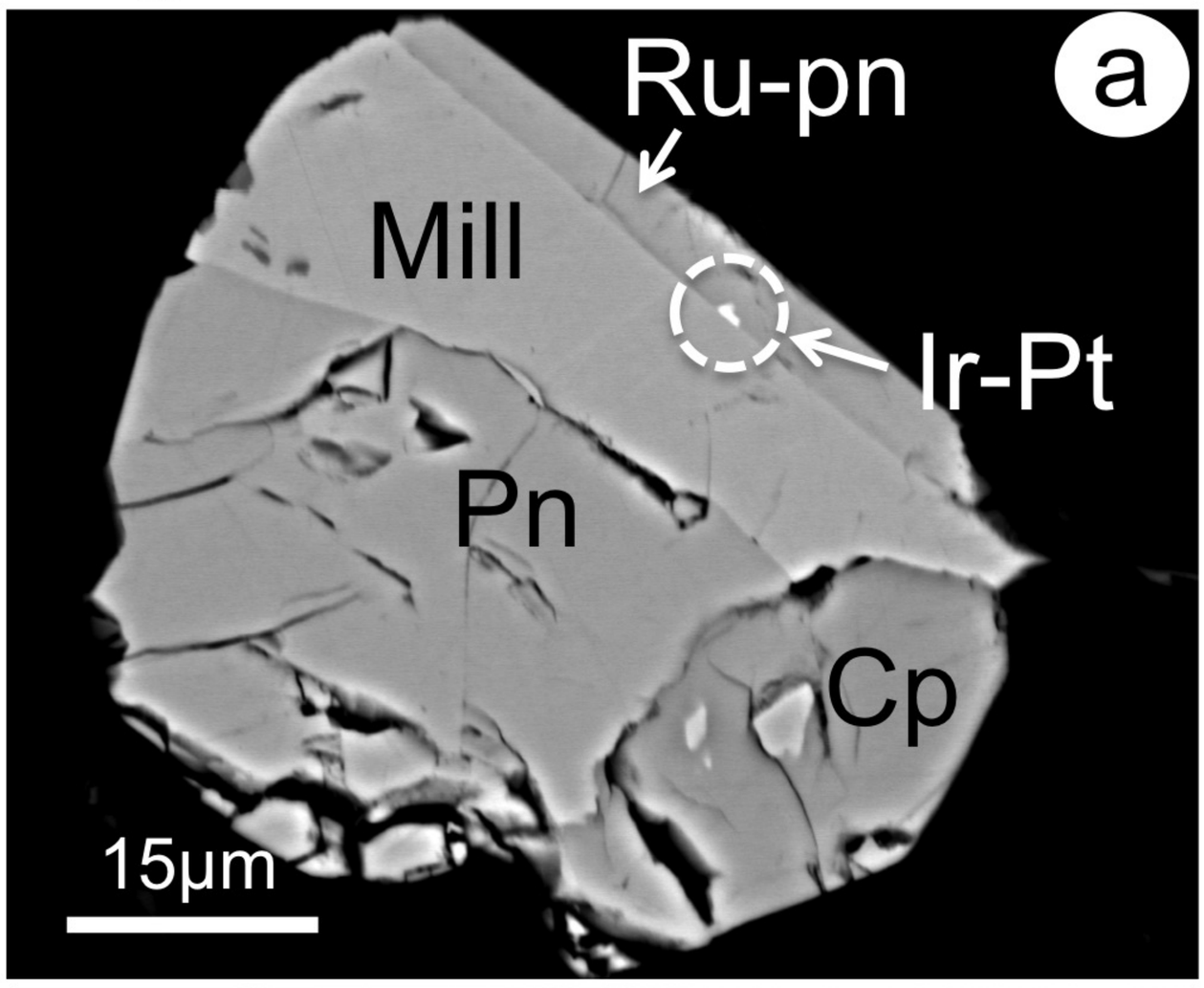

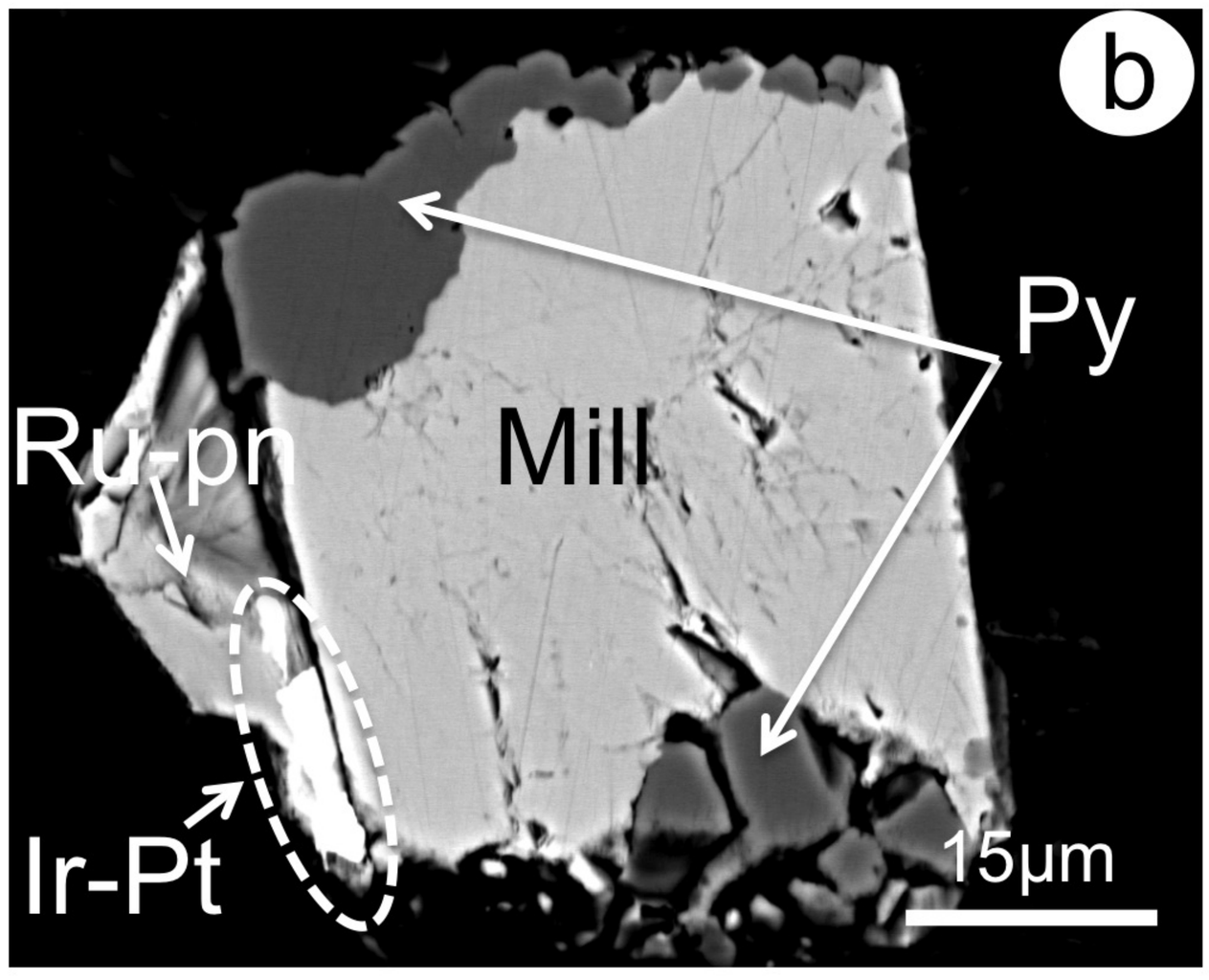

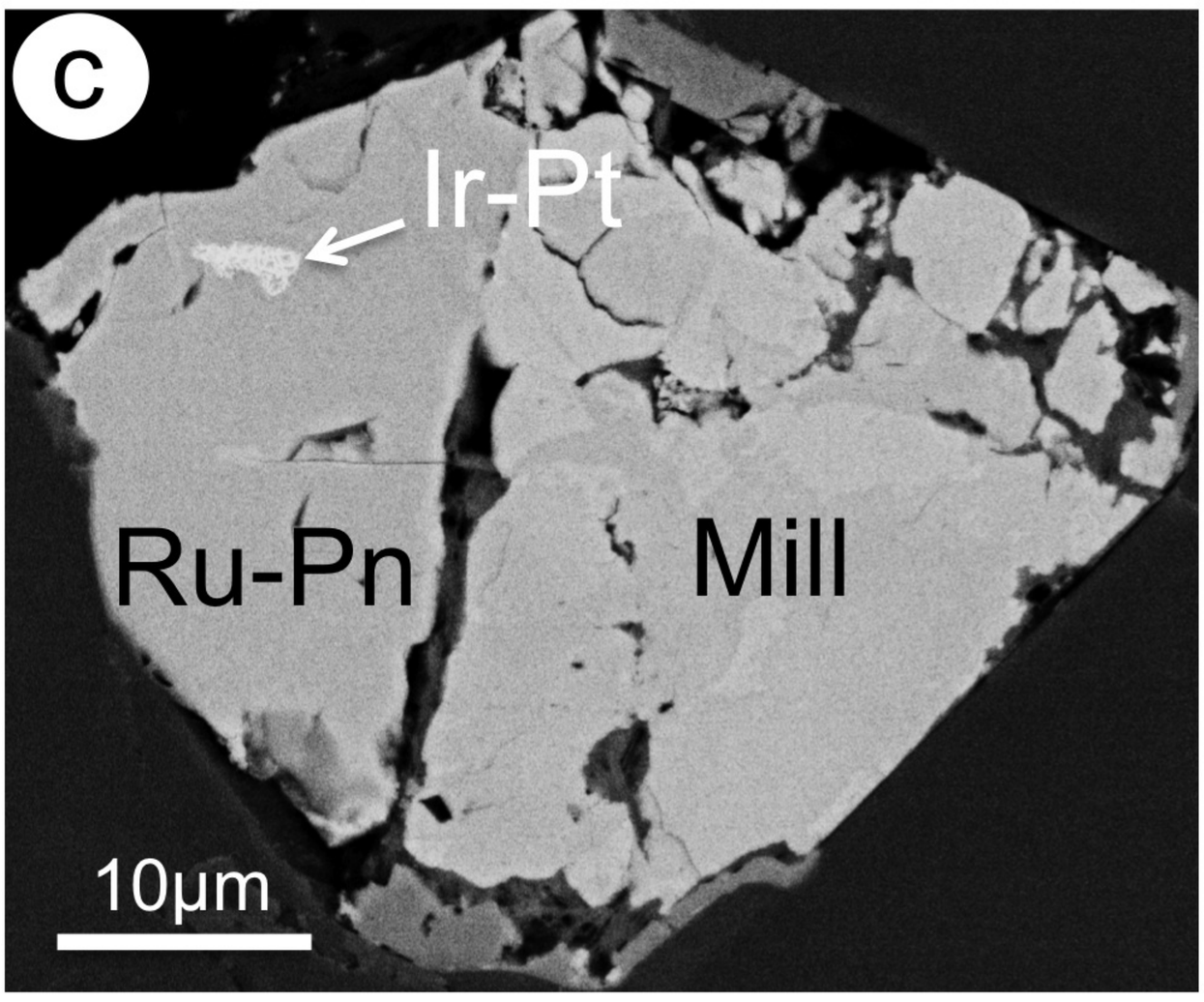

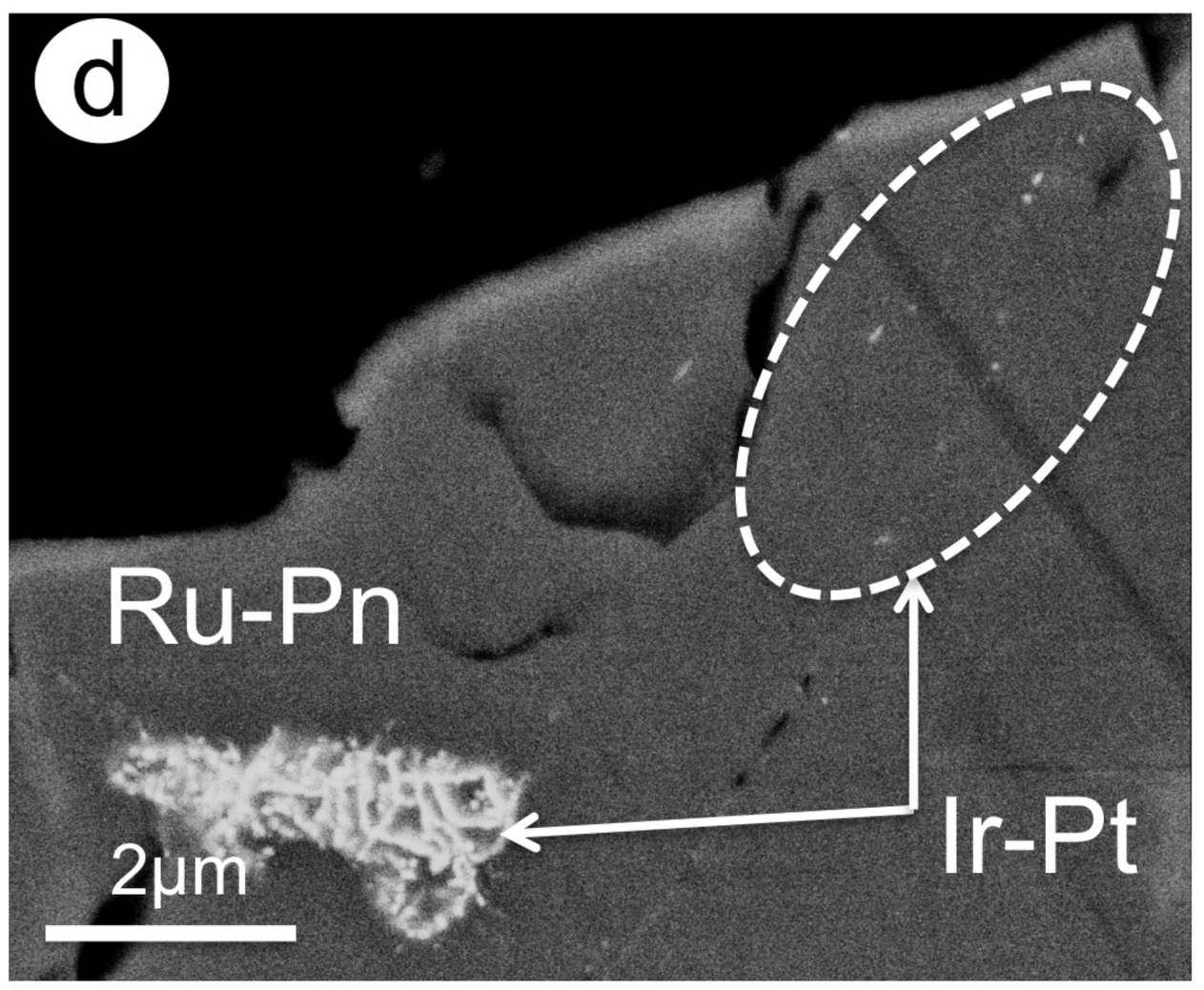

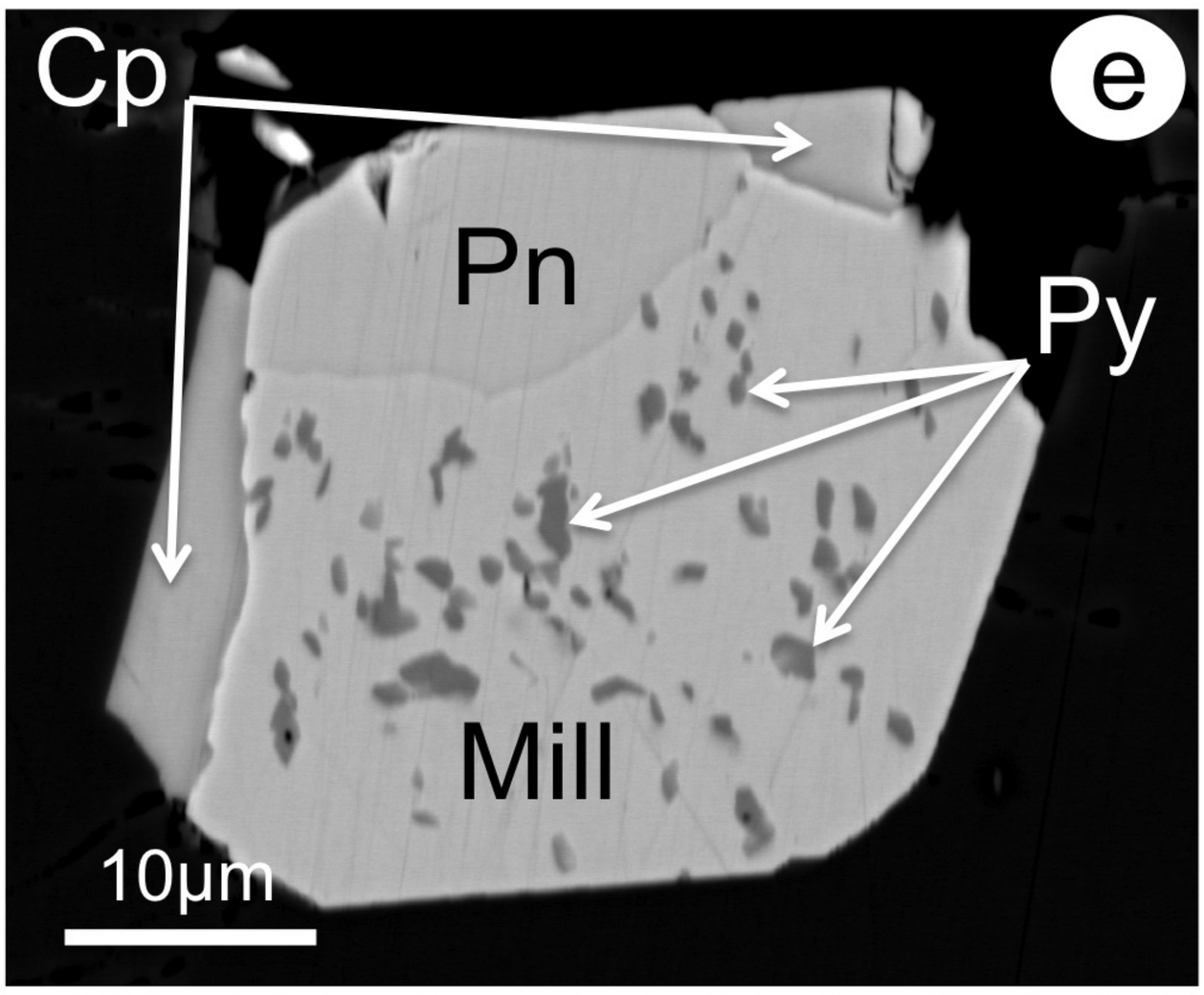

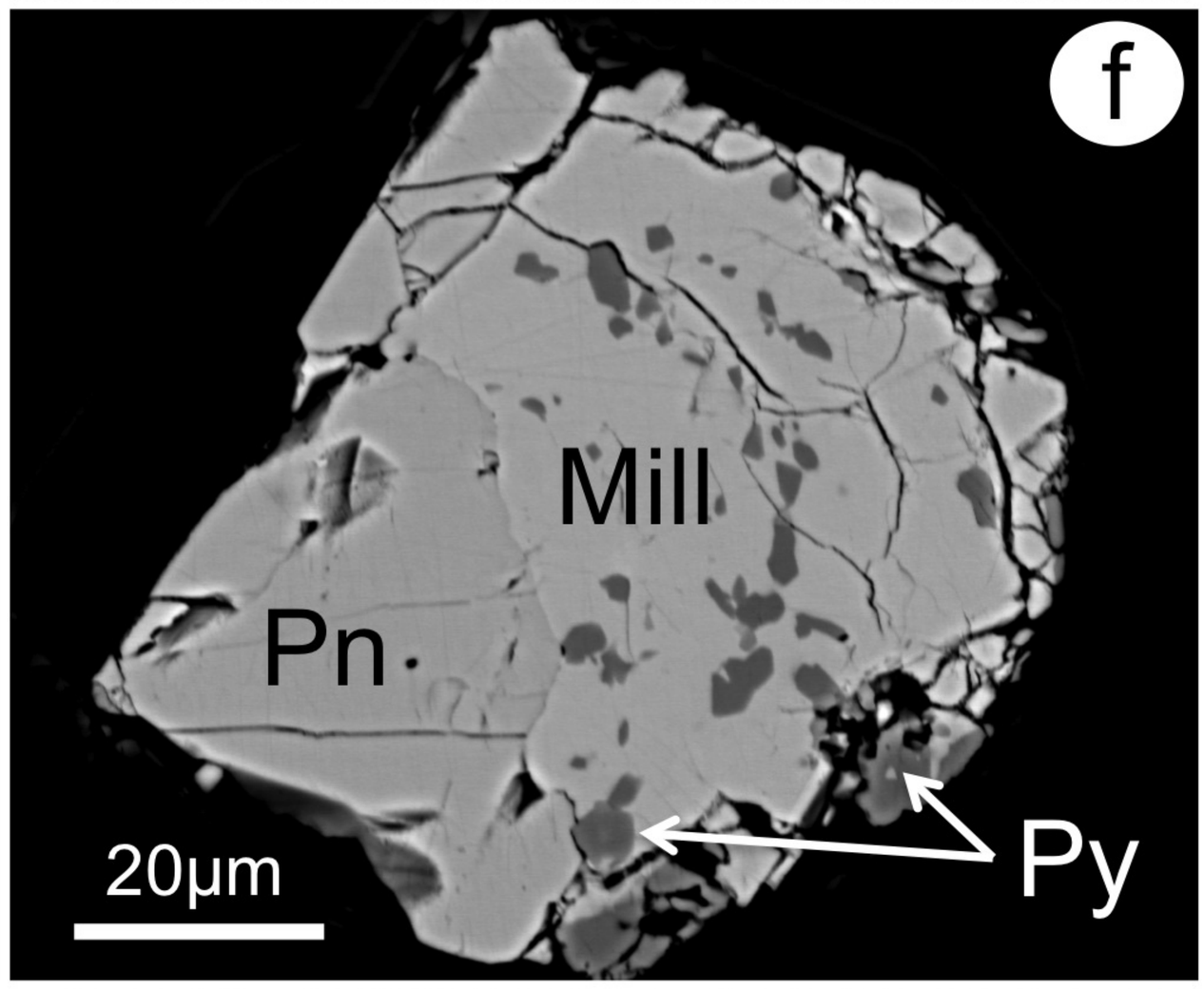

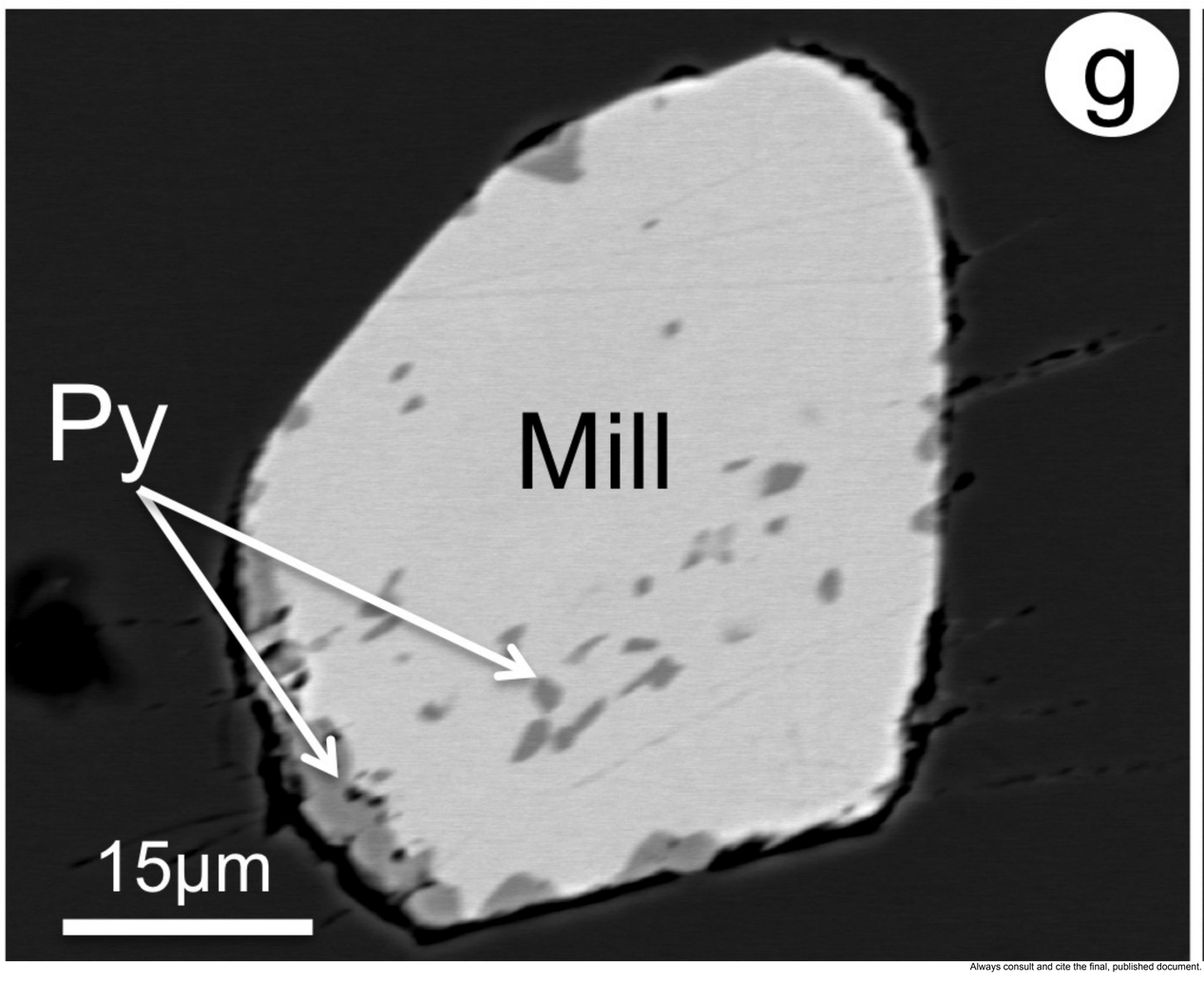

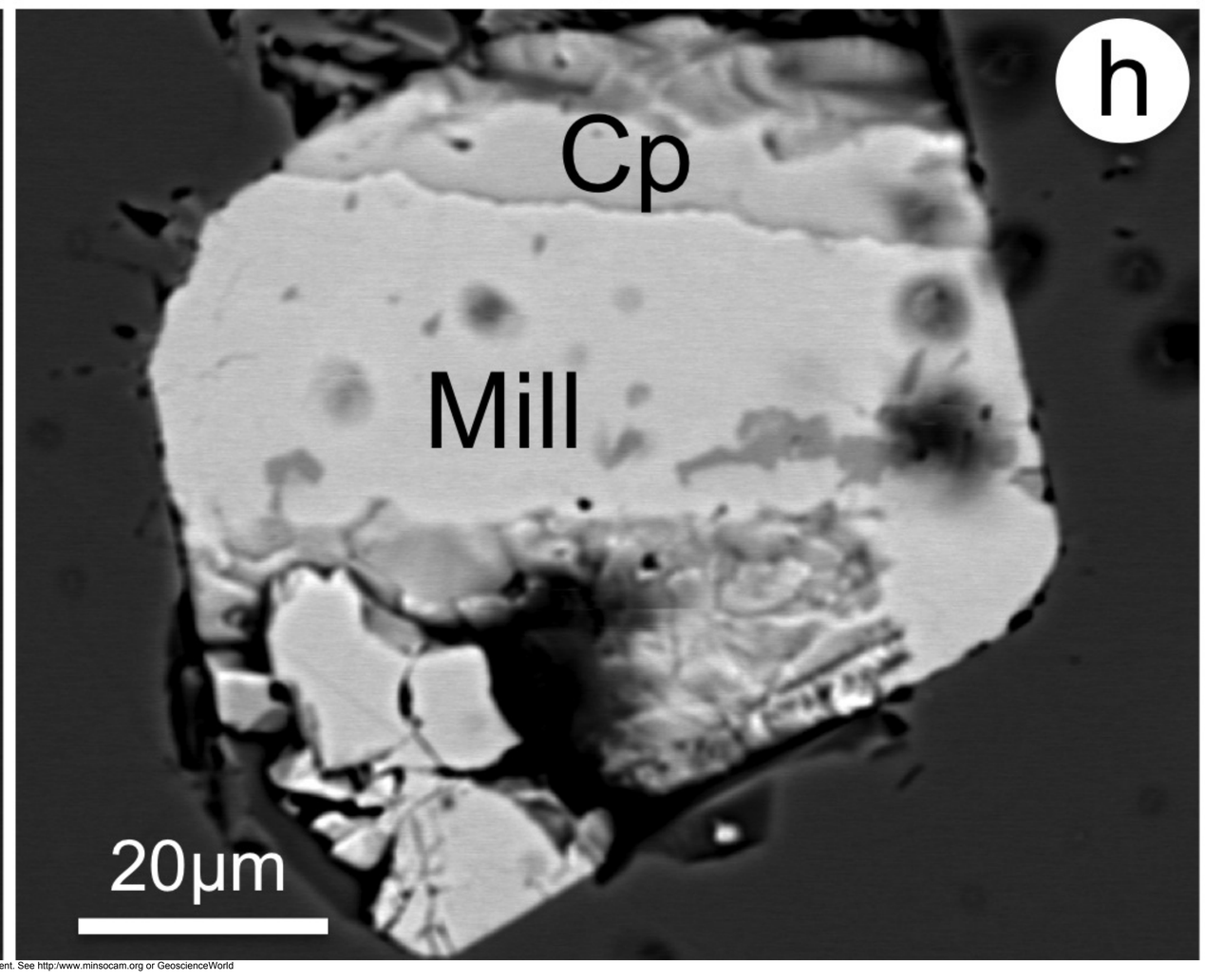

This is a preprint, the final version is subject to change, of the American Mineralogist (MSA)
Cite as Authors (Year) Title. American Mineralogist, in press.
DOI: https://doi.org/10.2138/am-2018-6424

Figure 3

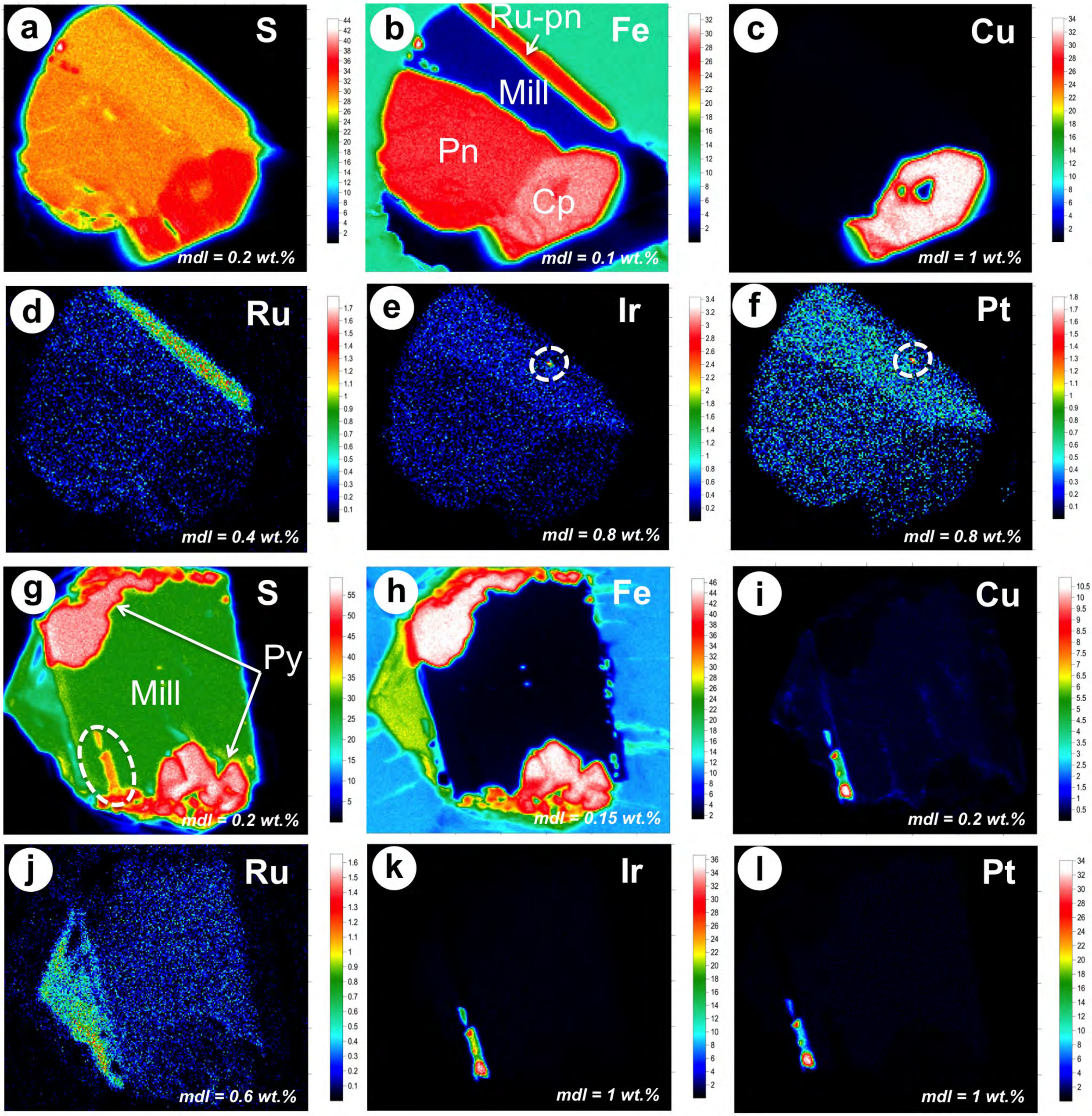

This is a preprint, the final version is subject to change, of the American Mineralogist (MSA)
Cite as Authors (Year) Title. American Mineralogist, in press.
DOI: https://doi.org/10.2138/am-2018-6424

Figure 4

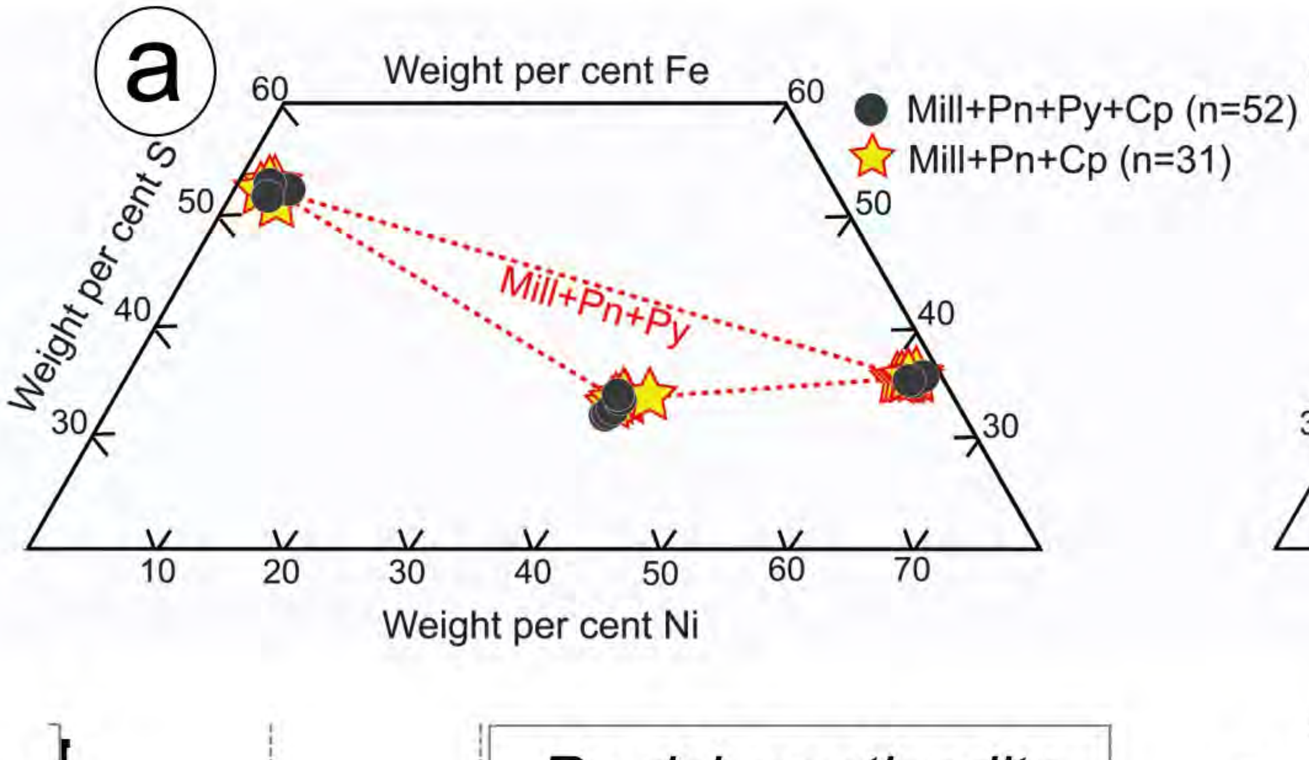

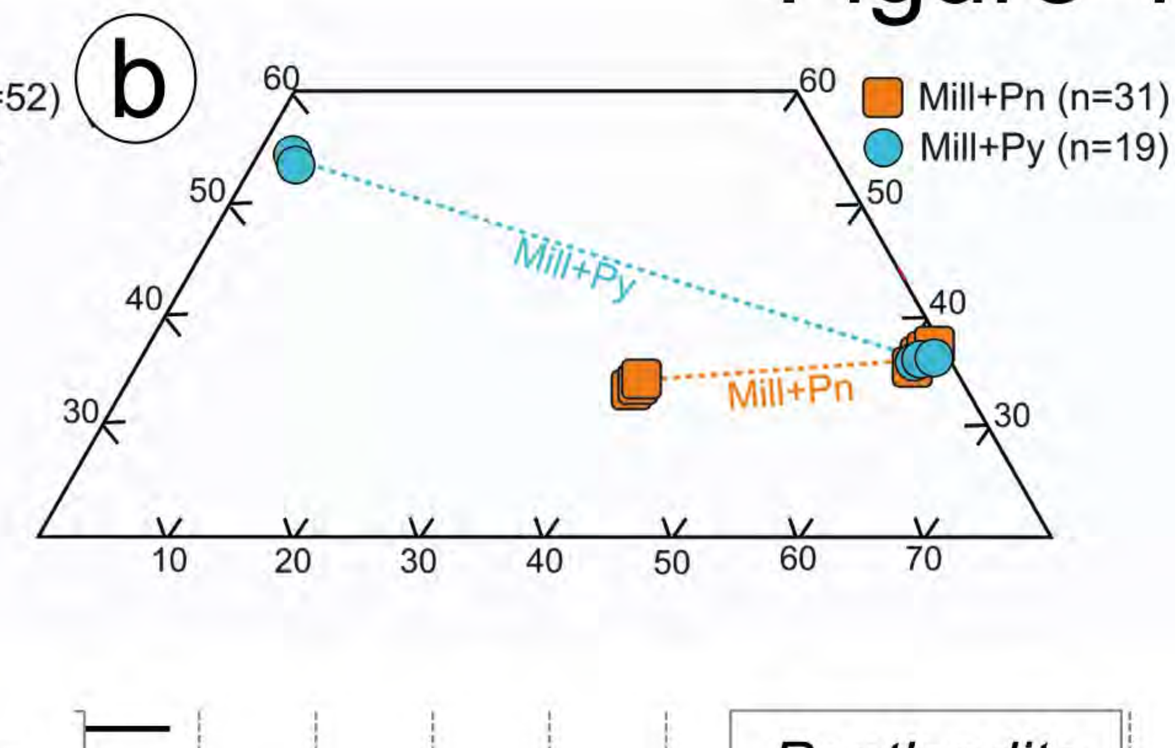

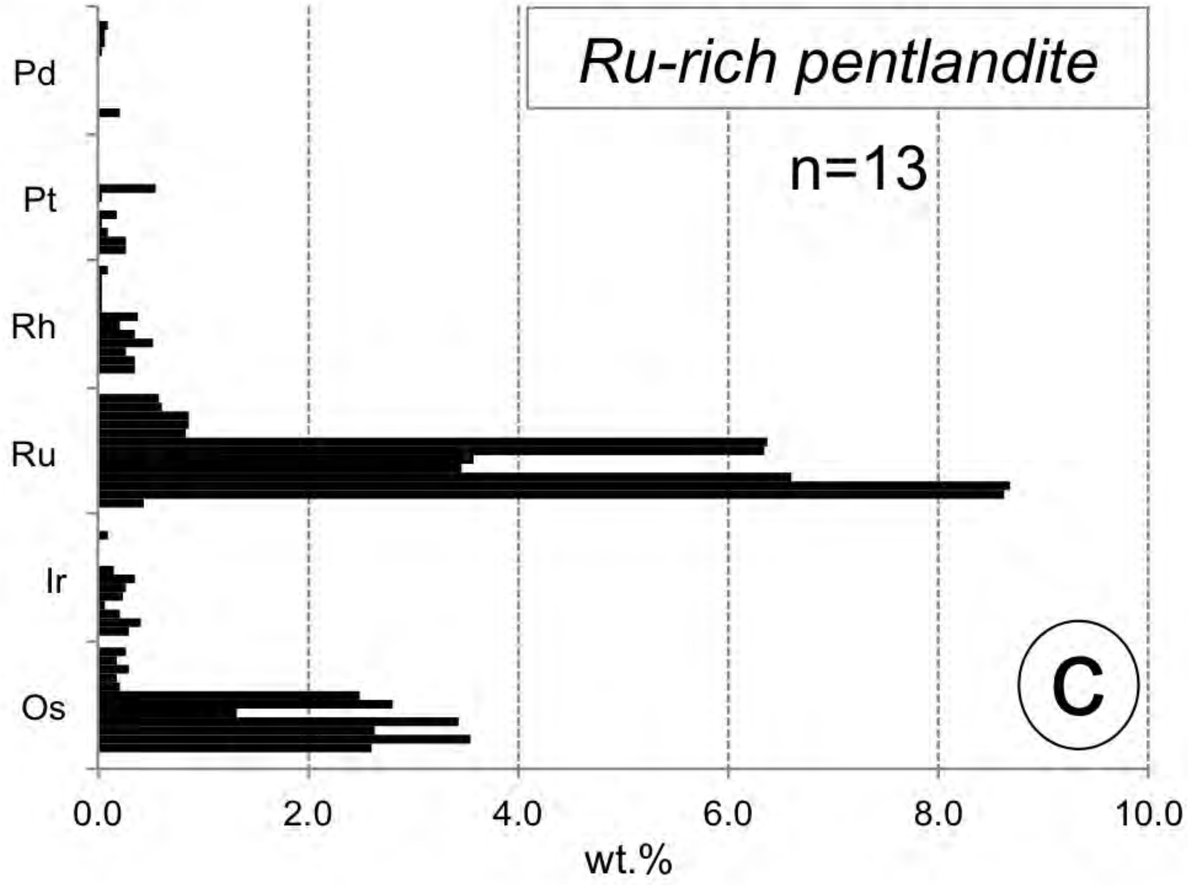

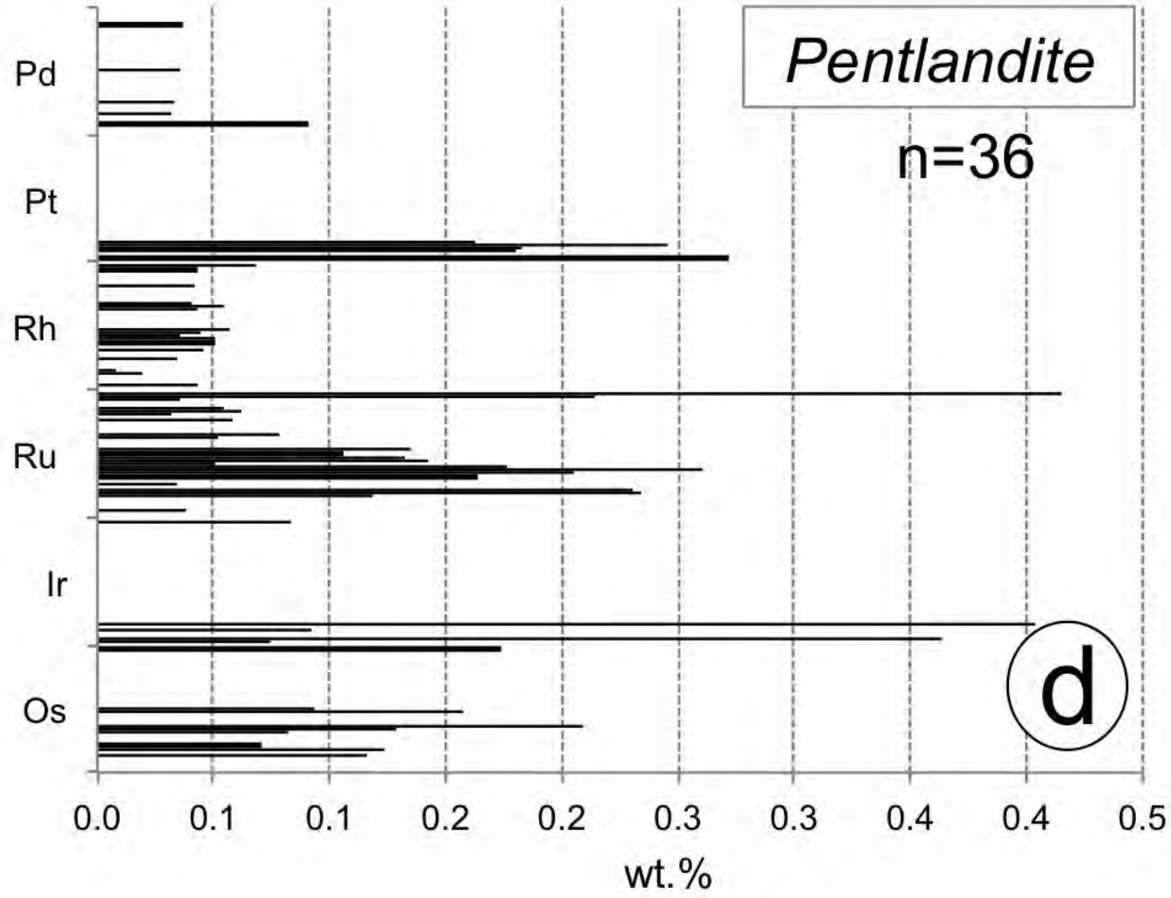

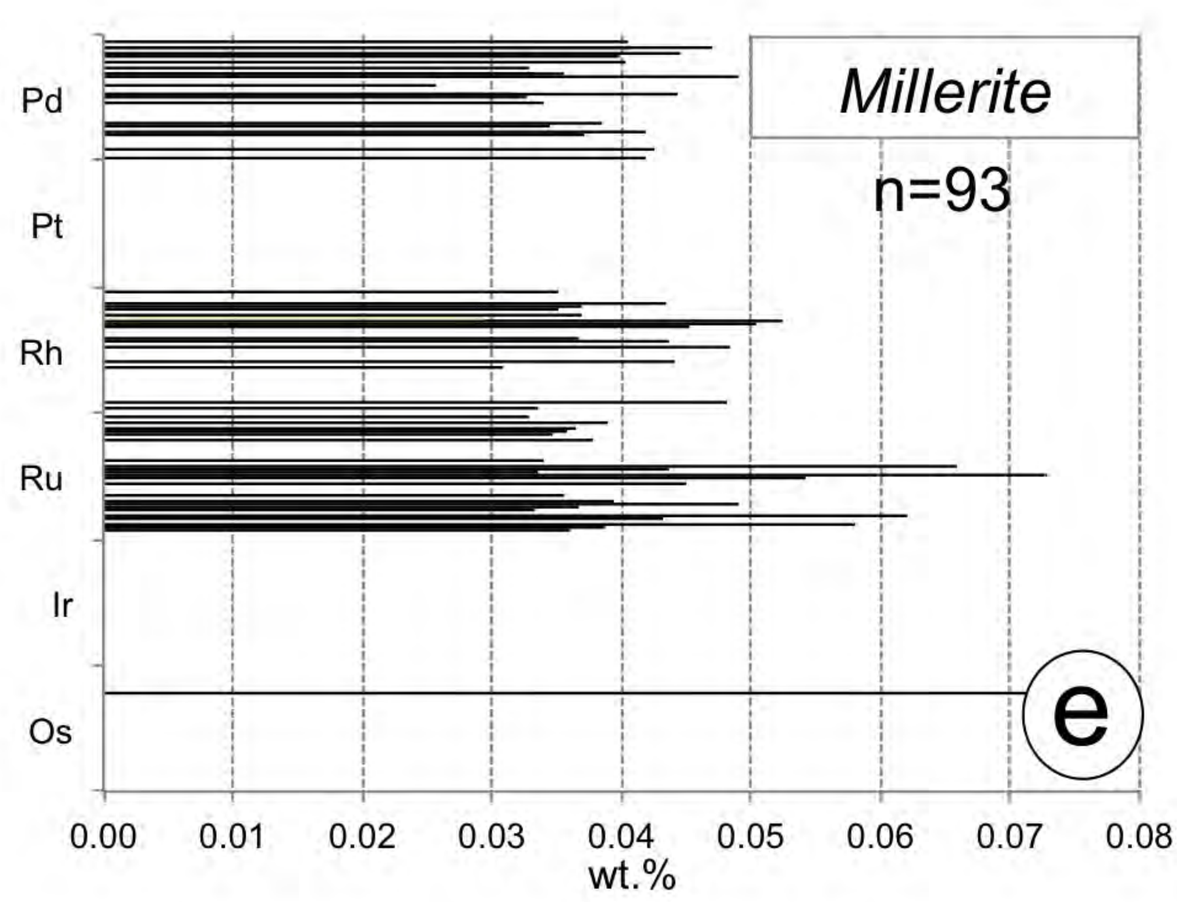

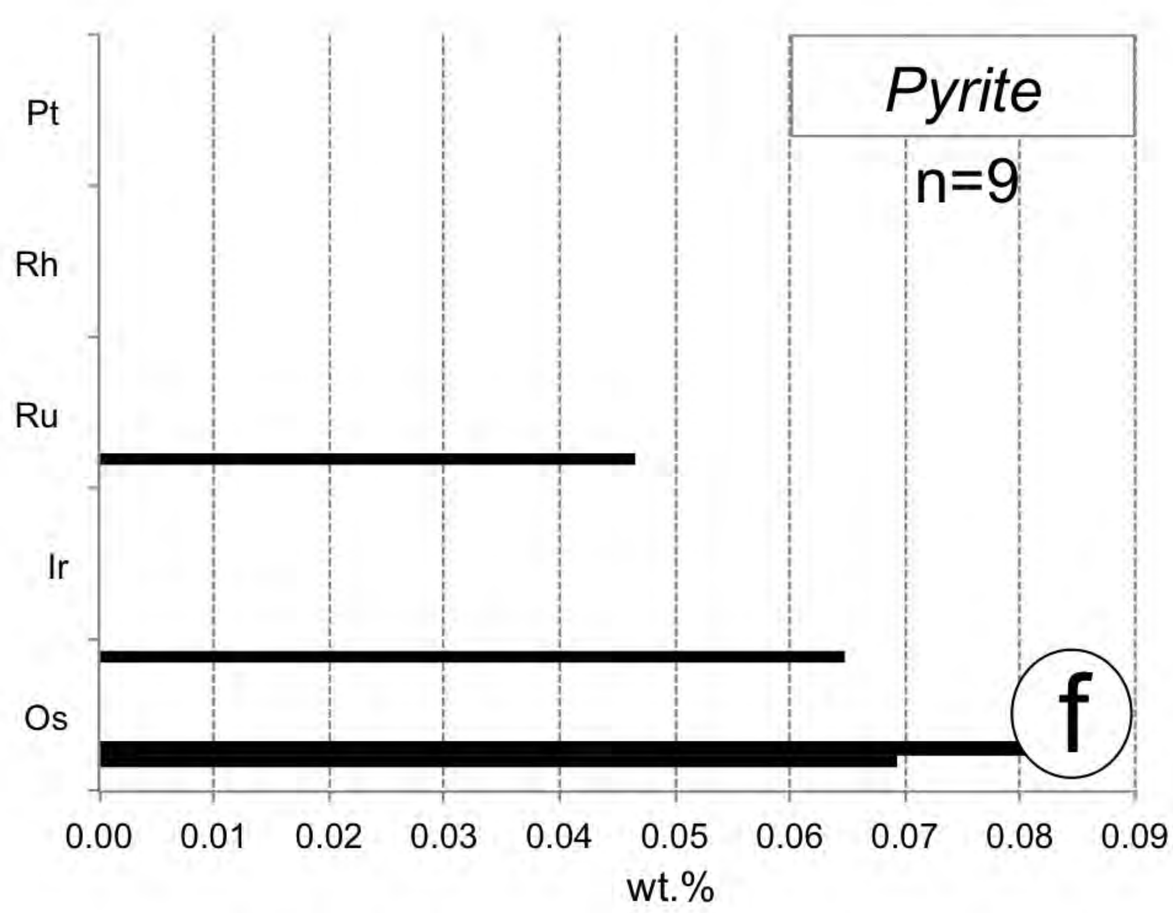

This is a preprint, the final version is subject to change, of the American Mineralogist (MSA)
Cite as Authors (Year) Title. American Mineralogist, in press.
DOI: https://doi.org/10.2138/am-2018-6424

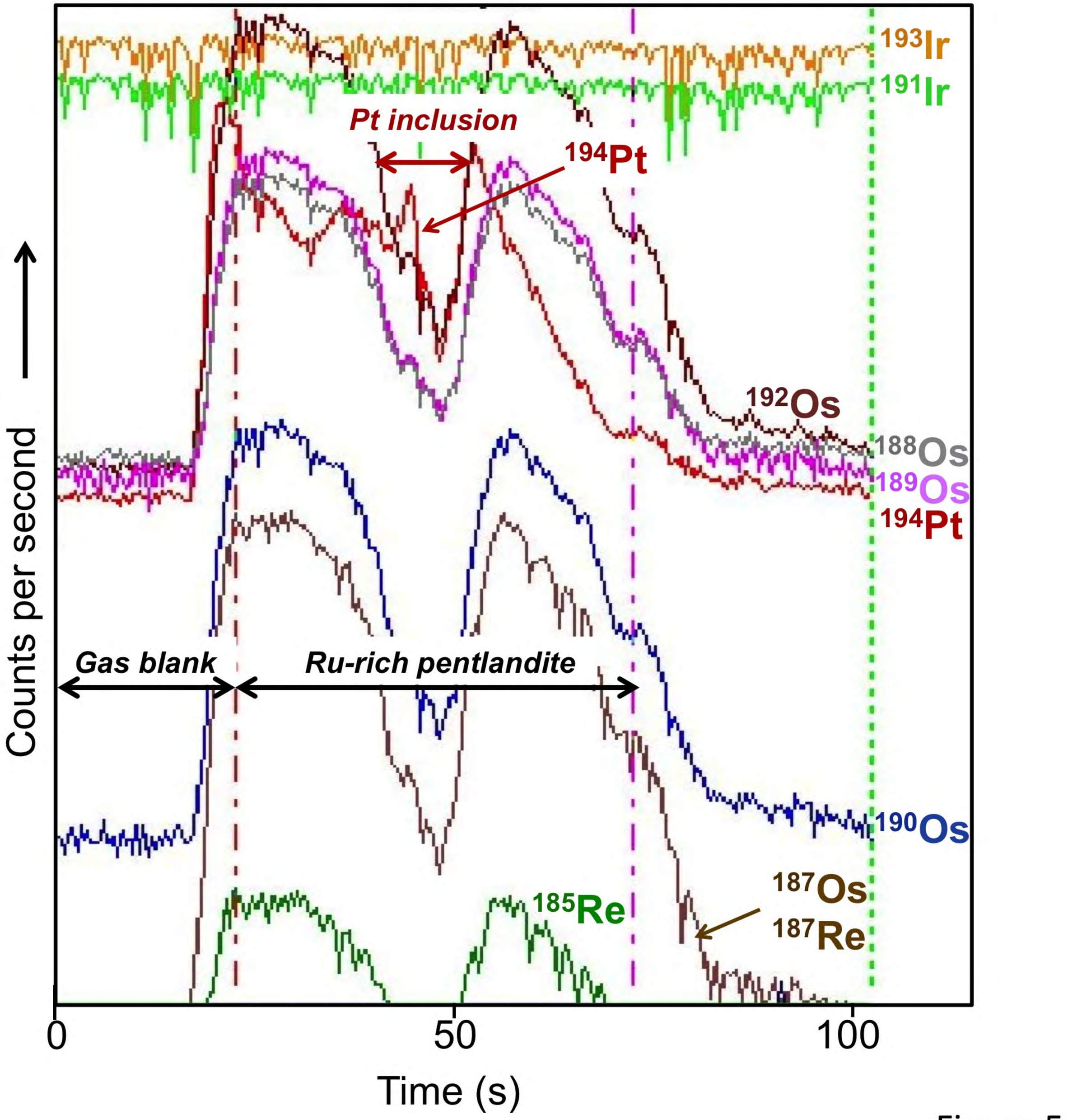

Figure 5

This is a preprint, the final version is subject to change, of the American Mineralogist (MSA)
Cite as Authors (Year) Title. American Mineralogist, in press.
DOI: https://doi.org/10.2138/am-2018-6424

Figure 5

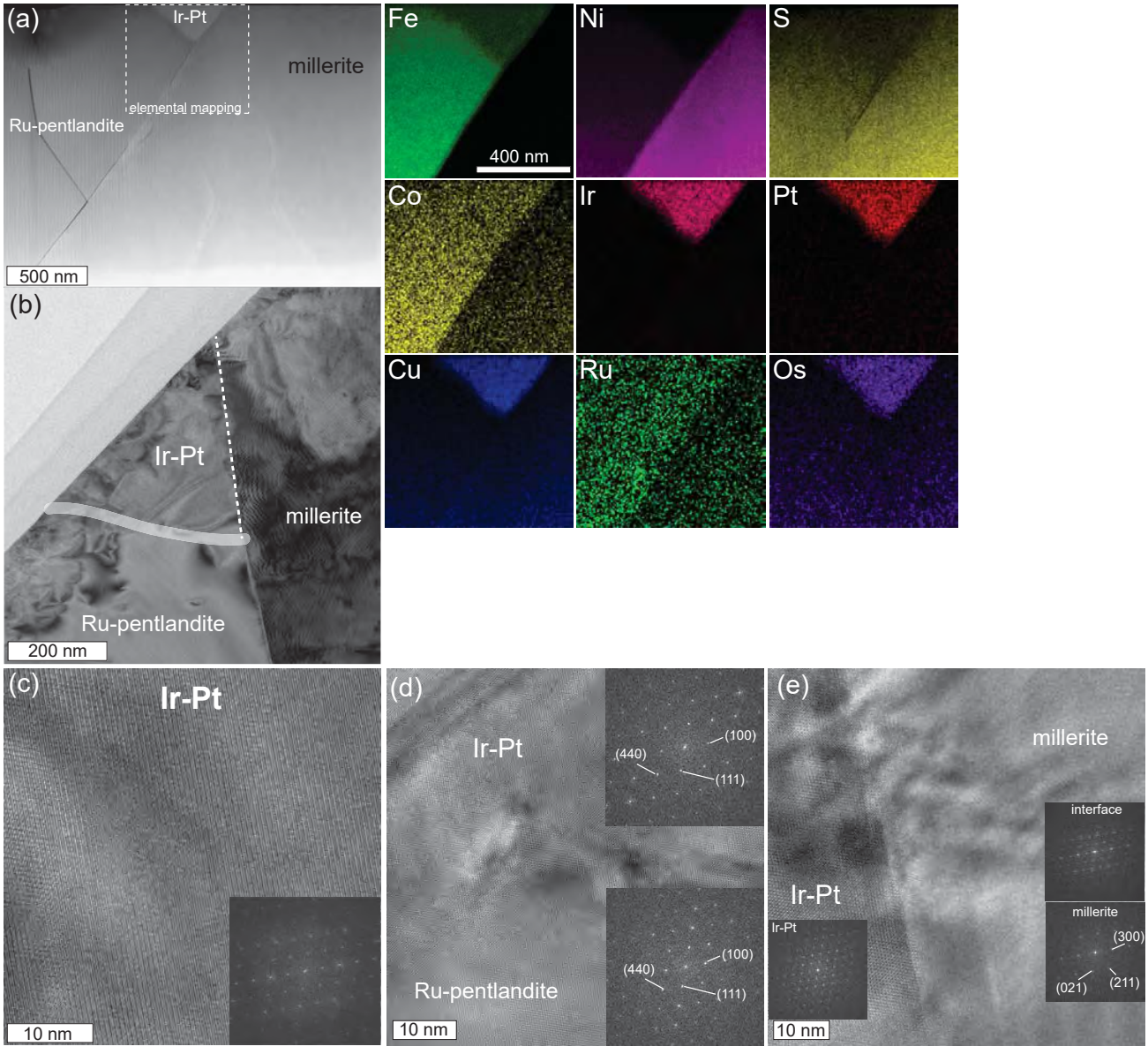

Figure 7

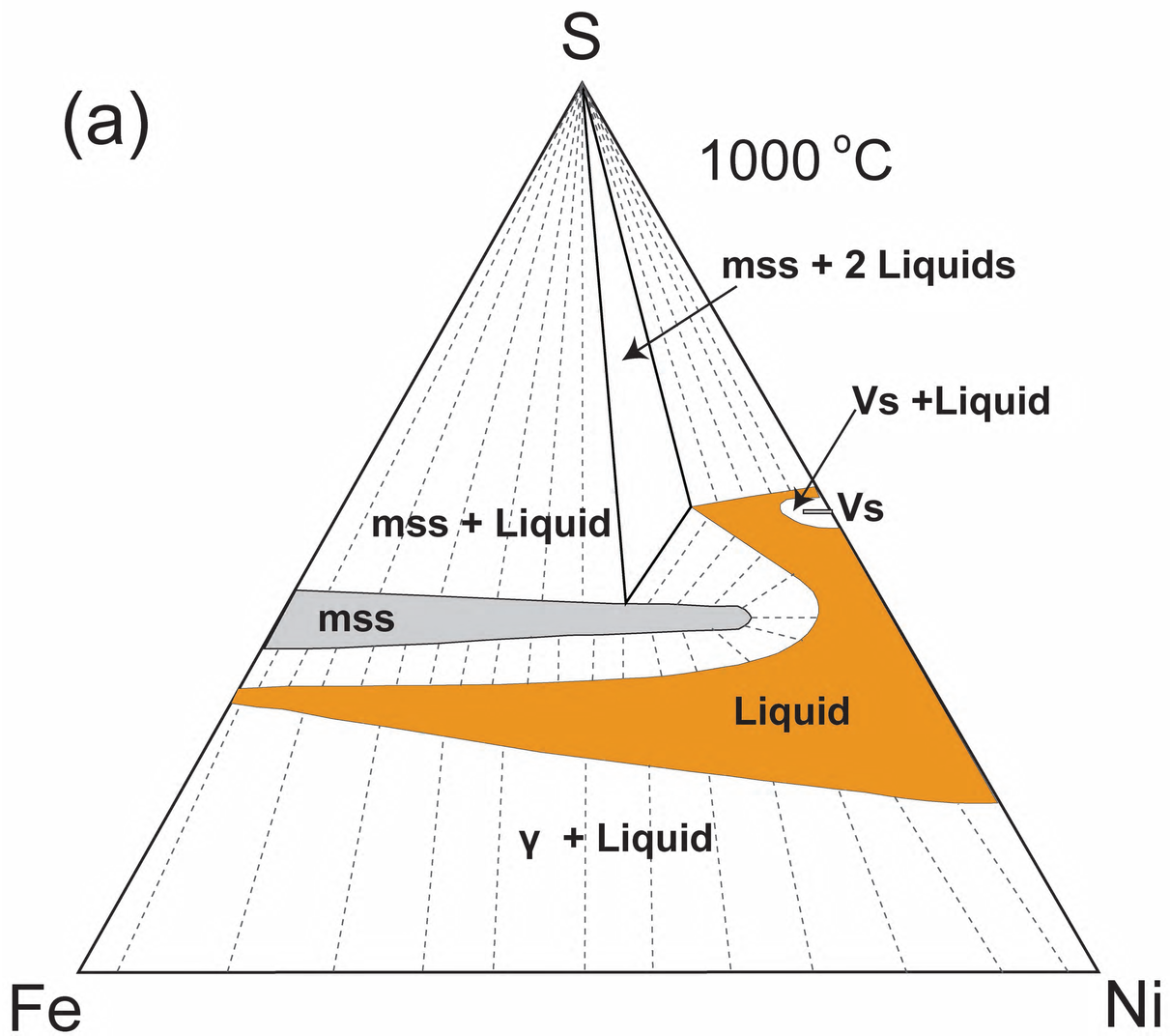

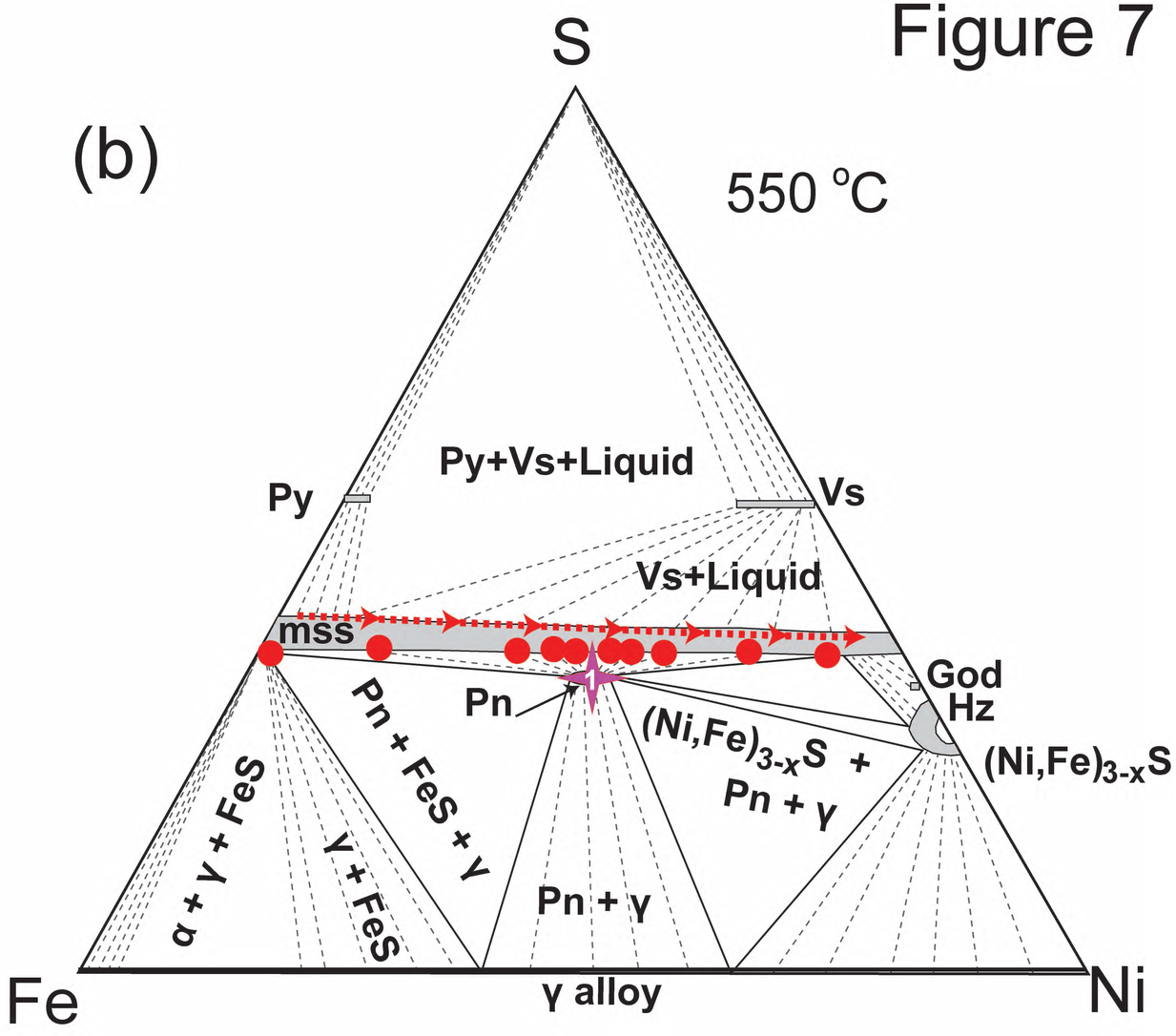

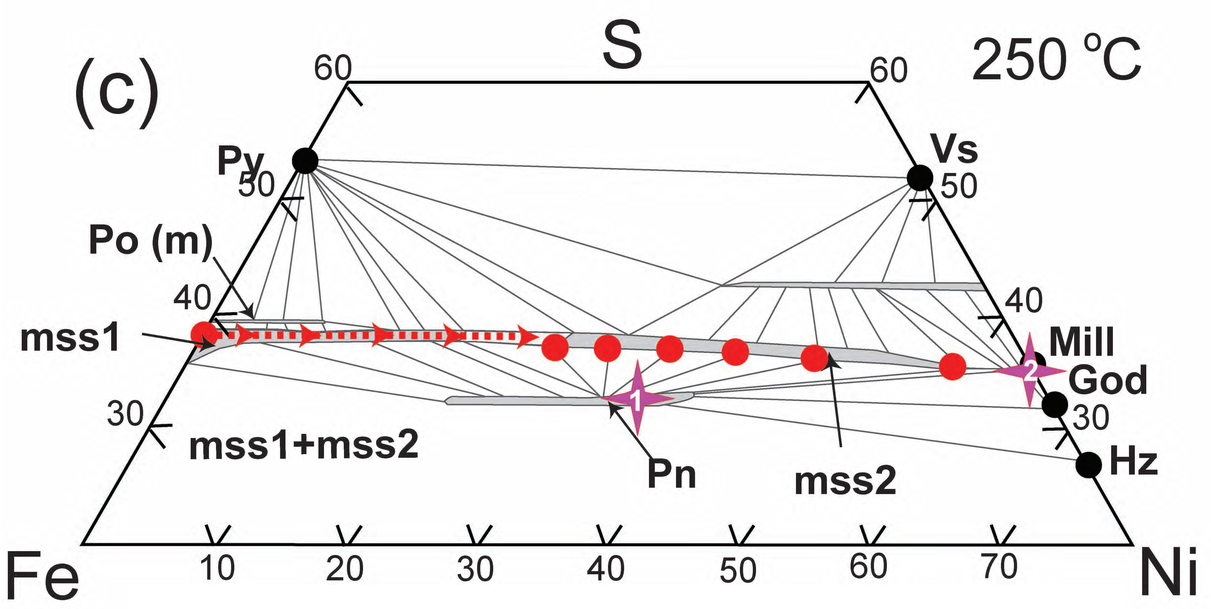

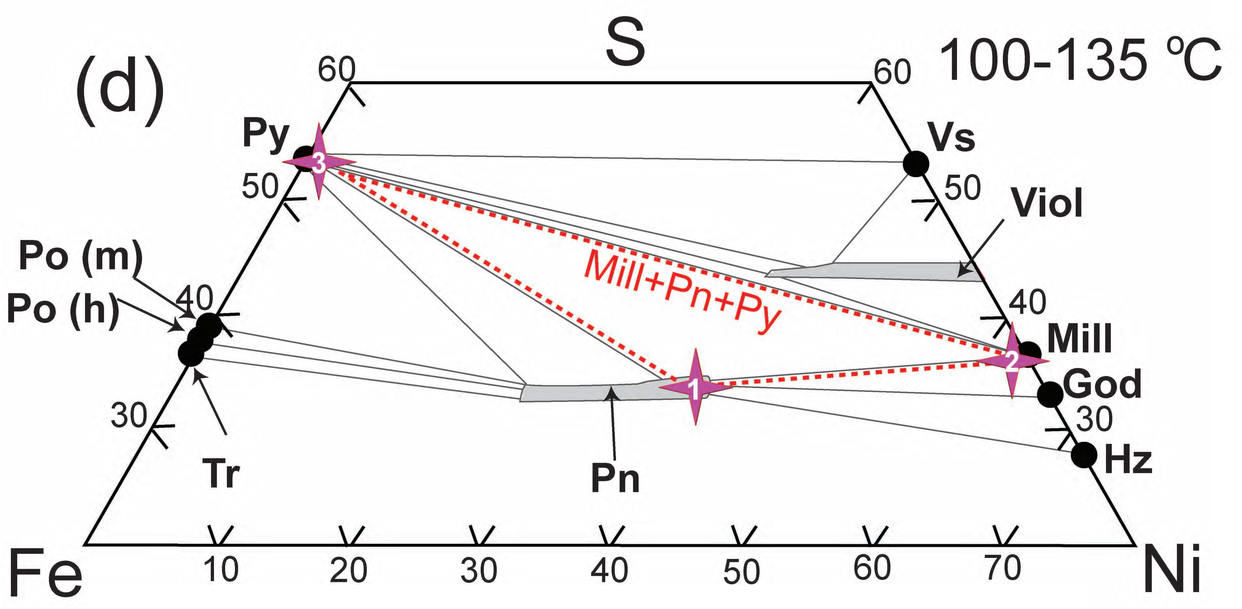

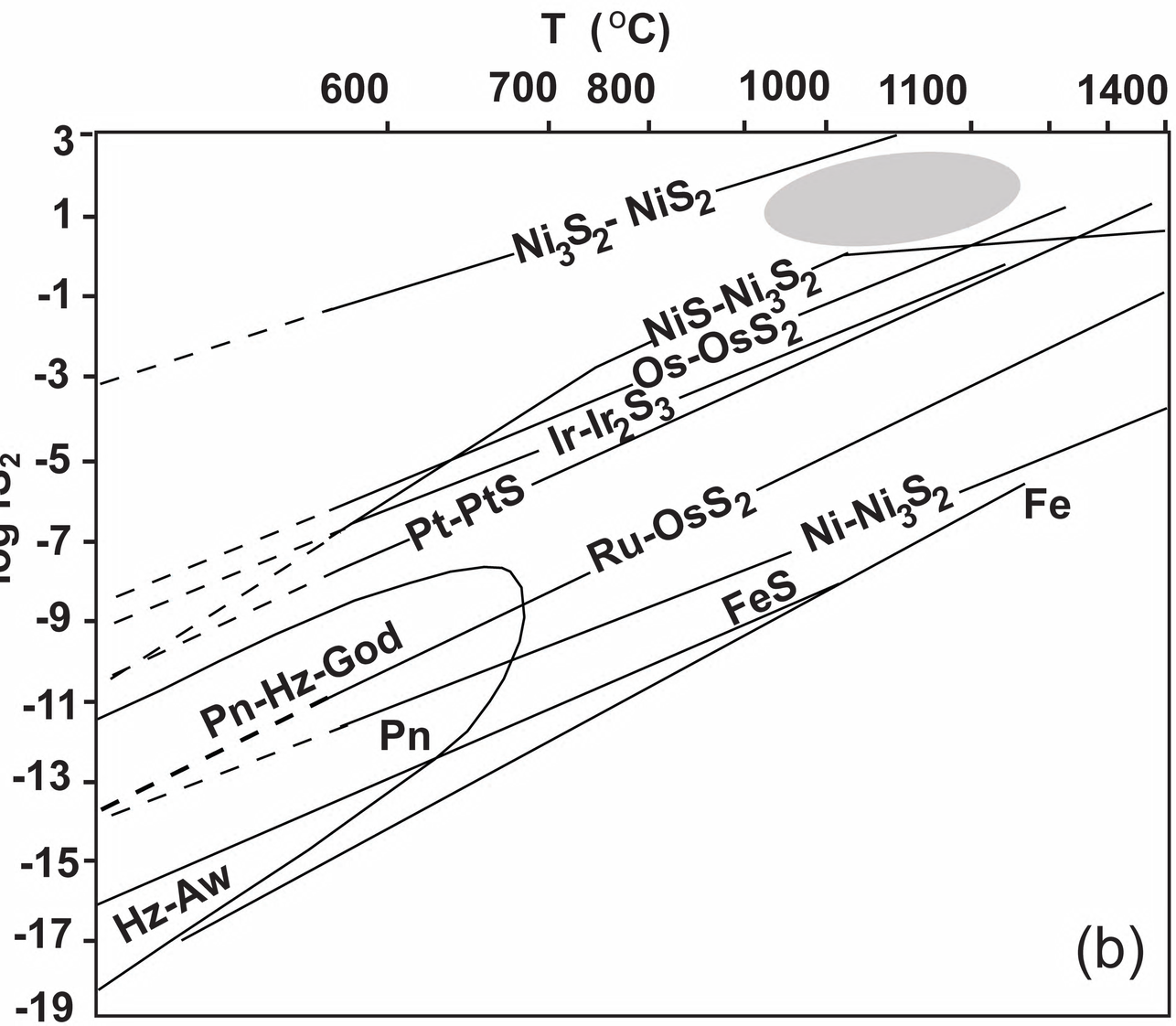

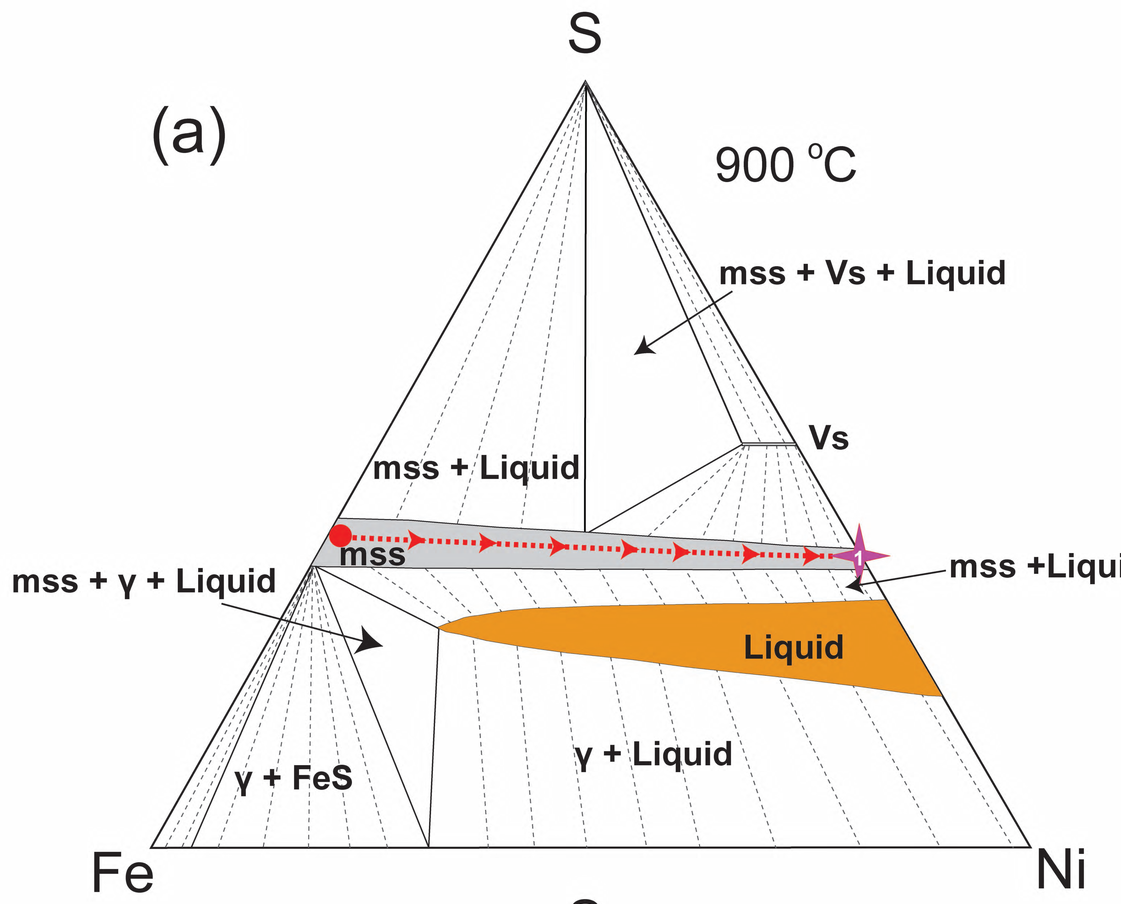

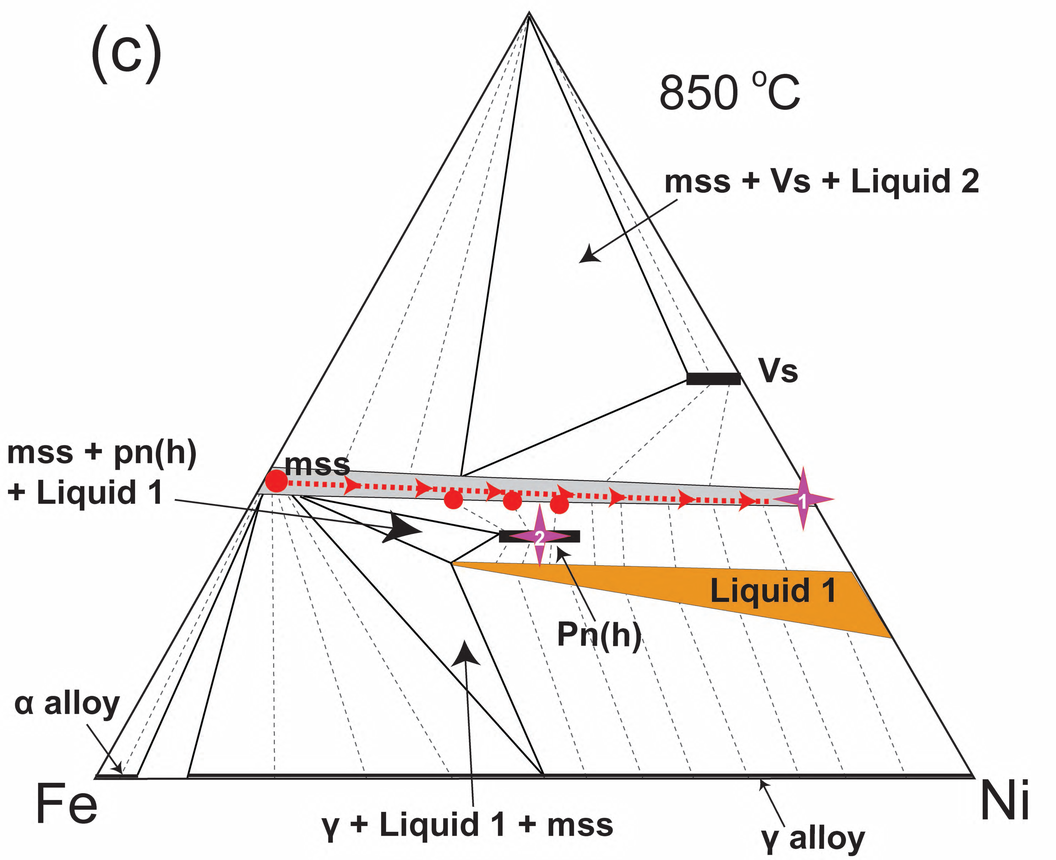

Figure 8

Figure 9